TITLE: Biophysically relevant network model of the piriform cortex predicts odor frequency encoding using network mechanisms

Abbreviated Title: Piriform cortex encodes odor frequency

Authors: Ankit Kumar[1], Om Chaudhari[2], Manan Jindal[3], Ashutosh Modi[2], Debanjan Dasgupta[1*]

Affiliations: [1]Neural Circuit Dynamics Lab, Department of Biological Sciences and Bioengineering, Indian Institute of Technology, Kanpur, 208016, India; [2]Department of Computer Science and Engineering, Indian Institute of Technology, Kanpur, 208016, India; and [3]Department of Electrical Engineering, Indian Institute of Technology, Kanpur, 208016, India

***To whom correspondence should be addressed:** Debanjan Dasgupta at debanjand@iitk.ac.in

Abstract

Olfactory-guided animals utilize fast concentration fluctuations in turbulent odor plumes to perceive olfactory landscapes. Recent studies demonstrate that the olfactory bulb (OB) encodes such temporal features present in natural odor stimuli. However, whether this temporal information is encoded in the piriform cortex (PCx) remains unknown. Hence, we developed a biophysically relevant PCx network model and simulated it using previously recorded *in vivo* activities of mitral and tufted cells in response to 2Hz and 20Hz odor frequencies for three odor mixtures. Analysing the single-cell activity across trials revealed that individual pyramidal neurons (PYRs) were ineffective at distinguishing between 2Hz vs. 20Hz. However, the trial-averaged activity of the PYRs population could discriminate between the two frequencies significantly. Moreover, using log-likelihood scores we further discovered that odor frequency discrimination happened through a highly distributed mechanism among the PYRs. 1-D convolutional neural network (CNN) models trained and tested on PYRs' activities achieved discrimination accuracies up to 95%. Using virtual synaptic knockout models, we found that eliminating either feedback or feedforward inhibition onto PYRs improved the decoding accuracy across all odor conditions. Conversely, eliminating recurrent excitation among PYRs or simultaneously eliminating recurrent inhibition among both interneuron types degraded the accuracy. Removing recurrent connections within individual interneuron populations had minimal effects on the performance. Overall, our PCx model demonstrates that it can discriminate between 2Hz and 20Hz odor stimuli, with a bidirectional capability of performance modulation by specific circuit motifs. These findings predict that the piriform cortex encodes and processes temporal features of odor stimuli.

NEW & NOTEWORTHY

We simulated the first biophysically relevant network model of the piriform cortex (PCx) to show differential encoding of odor frequencies at 2Hz and 20Hz. 1D convolutional neural networks demonstrated a distributed role of pyramidal cells in odor frequency decoding. Eliminating

feedforward or feedback inhibition improves frequency discrimination, while eliminating recurrency impairs it. Specific circuit motifs, not just baseline activity levels, determine odor frequency representation. Overall, our results predict the PCx's capacity for temporal odor processing.

Keywords: Circuit motifs; odor frequency; olfaction; piriform cortex

Introduction

In natural olfactory environment, odorant molecules travel as odor plumes due to the turbulence of natural airflow (1–4). These odor plumes are characterized by rapid concentration fluctuations of odorant molecules over space and time (4–8). It has been observed that such odor plumes carry crucial spatial information about odor source location, embedded in their temporal structure (1,3,9). Olfactory-guided animals can perceive the temporal structure of odors (1,3,9–11), and recent reports indicate that humans can perceive such stimuli as well (12). Early olfactory regions in the nervous system, like the antennal lobe in insects (13–18) and the olfactory bulb (OB) in mammals, can represent these temporal features (19,20). However, it is unknown whether this information can be encoded in higher olfactory cortical areas like the piriform cortex (PCx).

Owing to the slow signal transduction through GPCR-based odorant receptors, olfaction has largely been thought to be devoid of high-frequency temporal features of odor stimuli (21). However, studies in invertebrates (16,17) and more recently in mice (3,8,11,19,20) and humans (12) have shown that different temporal features of odor stimuli can be perceived and encoded at least in the early olfactory system. One of the main cortical areas associated with olfaction is the PCx which has largely been associated with encoding of odor identity and intensity (22,23). The recurrent network of the PCx is responsible for olfactory sensory processing, which includes shaping the ensembles of odor-identity encoding piriform neurons (24), gain control, pattern separation and pattern completion, as well as odor learning and memory formation (25–29). Moreover, PCx, through its cortical feedback axons, provides the OB with efficiently formatted and decorrelated information about diverse odorant mixtures and concentrations (30). However, we completely lack an understanding of whether PCx's

recurrent circuitry can encode odor temporal features such as frequency of odor concentration fluctuations. Hence, given the importance of odor temporal information in various ethological behaviors and the known involvement of the olfactory cortex (31,32), we investigated whether the PCx is capable of encoding different temporal features present in naturalistic odor stimuli.

To investigate this, we developed a biophysically constrained network model of the PCx. We analysed pyramidal cells (PYRs) activity in response to three odorant mixtures presented at 2Hz and 20Hz frequencies. Additionally, we simulated various PCx synaptic knockout models to determine the extent to which each circuit motif influences the network's frequency discriminating capacity. Our findings demonstrate that the PCx network can effectively discriminate between 2Hz and 20Hz odor frequencies. Eliminating direct feedforward or feedback inhibition onto the PYRs enhanced the frequency decoding capacity of the PCx network model, whereas removing recurrent excitation onto the PYRs or disinhibition among both feedforward and feedback interneurons impaired this capacity. In contrast, the odor frequency decoding accuracy was minimally affected by the synaptic disconnections of the intra-feedforward or intra-feedback interneurons. Overall, our study predicts that the PCx network can perform odor frequency discrimination through network mechanisms. Furthermore, the phenomenon can be modulated bidirectionally by the different synaptic motifs in the network.

Materials and Methods

Model

The code was written in Python using the NEURON 8.0.2 simulation environment (33) and executed using Conda/Virtual Environments. The integration time step for the simulations was 0.025ms.

Model Architecture

The piriform cortex model consisted of three types of cells: 500 excitatory pyramidal cells (PYRs), 50 feedforward inhibitory neurons (FFINs), and 50 feedback inhibitory neurons (FBINs). All synaptic connections within the network were randomly assigned, regardless of cell location. Previously

recorded *in vivo* activity from 20-50 unique mitral/tufted cells (M/Ts) from the olfactory bulb in response to different stimulus conditions was used as input to simulate the PCx network model. These spiking activities were duplicated as needed to generate an M/T cell population of size ~22.5% of PYRs. Each pyramidal cell received input from 20% of mitral cells, as previously modeled (34). Each pyramidal cell was connected to 20% of the total pyramidal cell population (34) through proximal apical dendrites (24). The FFINs projected to the distal apical dendrites of pyramidal neurons (35–37). Each PYR was inhibited by 30% of the FFINs (38). Each FFIN received inputs from 40% of M/T cells (36,37). Each FBIN was excited by 18% of the PYRs and each PYR was inhibited by 35% of the FBIN network through somatic inhibition (37). Each FBIN received inhibitory inputs from 10% of FBINs, while each FFIN received inhibitory inputs from 40% of FFINs.

Neuron and Electrophysiological parameters

Pyramidal (PYR) neuron model:

Each PYR was composed of a soma and five dendritic sections. Both the length and diameter of the somatic section were 29 µm. The length of all dendritic sections was 100 µm. The diameters of all dendritic sections 1 to 5 were 2.57, 1.77, 1.2, 0.8, and 0.5 µm, respectively (Fig. S1A). Here, dendritic section 5 was considered the distal apical dendrite. The charge balance equation for each neuronal compartment is described by:

$$C_M \frac{dV}{dt} + I_K = I_A \qquad (1)$$

Where:

C_M is 1 µF/cm^2

V is membrane voltage

I_K is the sum of ionic currents that pass through the membrane and

I_A is the current entering from adjacent regions.

Equations governing I_K are defined explicitly in the mod file of each ion channel mechanism. Ion channel mechanisms (*.mod files) can be compiled using NRNIVMODL of NEURON. The value of axial resistance (R_a) for each section of all neuronal types was 173 Ωcm. Each PYR section had sodium and delayed rectifier potassium channel mechanisms adopted from Migliore et al. (1999). Leak channels in PYRs were implemented using NEURON's built-in "leak" distributed mechanism. The maximum conductance of sodium, potassium, and leak ion channels was 0.5, 0.06, and 0.003 S/cm^2, respectively. The reversal potential of sodium, potassium, and leak ion channels was 50 mV, -85 mV, and -75 mV, respectively. The resting membrane potential (RMP) of PYRs was -74.1 ± 8.6 mV (mean ± SD) (40). The input resistance of PYR soma and its dendritic sections 1 to 5 were 79.84, 80.28, 84.94, 99.36, 137.58, and 246.18 MΩ, respectively (Fig. S2B) based on experimental data (40). The baseline spike rate of soma, dend1, dend2, dend3, dend4, and dend5 was 2.22 ± 0.98, 2.21 ± 1.27, 2.32 ± 1.2, 2.19 ± 1.16, 2.2 ± 1.4, and 2.67 ± 1.59 Hz (mean ± SD), respectively (Fig. S2D). The f-I curve (firing frequency vs. injected current) of PYRs (Fig. S2E) closely matched previous experimental results (41). PYR baseline noise was modeled using NEURON's "INGAUSS" mechanism with mean ± SD = 0 ± 0.092, which generates action potentials at a specified frequency. For a concise overview of these parameters refer to Table 1.

Feedforward (FF) and Feedback (FB) interneuron model:

FFINs and FBINs are represented as single somatic compartments. The length and diameter of FFINs were both 85 µm, while those of FBINs were 68 µm (Fig. S1B-C). The charge balance equation in the compartments of both neuronal types is described by the same Equation (1). FFINs and FBINs have sodium, potassium, and leak channel mechanisms adapted from Wang and Buzsáki (1996). For FFINs, the maximum conductance of sodium, potassium, and leak channels was 0.05 S/cm^2, 0.015 S/cm^2, and 0.000048 S/cm^2, respectively. The reversal potentials for sodium, potassium, and leak channels were 55 mV, -90 mV, and -72 mV, respectively. For FBINs, the maximum conductance of sodium, potassium, and leak channels was 0.05, 0.01, and 0.00014 S/cm^2, respectively. The reversal potentials for sodium, potassium, and leak channels was 55 mV, -90 mV, and -78 mV, respectively. The resting membrane potential of FFINs and FBINs were -72 ± 5.9 mV

and -77.8 ± 11.3 mV (mean ± SD), respectively (43). The estimated input resistance of FFINs and FBINs were 93.36 MΩ (Fig. S3B(III)) and 50.29 MΩ (Fig. S4B(III)) respectively (43). The current vs. firing frequency plots estimated from FFINs (Fig. S3D) and FBINs (Fig. S4D) corroborated previous experimental results (Suzuki and Bekkers, 2010). FFINs' and FBINs' baseline noise was also modeled using NEURON's "INGAUSS" function with 0 ± 2.3 and 0 ± 5 (mean ± SD), respectively. The baseline firing rates of FFINs and FBINs were 2 ± 1.14 Hz (Fig. S3F) and 6.55 ± 2.11 Hz (Fig. S4F), respectively. Simulations were conducted at a temperature of 33°C.

The somatic compartment of each cell type acts as an integration site for all inputs and generates spikes. This conceptual model of NEURON is based on the spike-triggered synaptic transmission in which a spike detected at the presynaptic terminal using a NetCon object causes conductance change at the postsynaptic terminal. A NetCon object connects a presynaptic variable, such as voltage, to a target synapse with a desired delay and weight (33). Every synapse was modeled using a two-state kinetic scheme described by rise time Tau1 and a decay time constant Tau2 and a reversal potential, E_N. All synapses were modeled using the NEURON's in-built "Exp2Syn" function. Synaptic latencies across different connection types were consistent with findings from Suzuki and Bekkers (2011). The synaptic parameters (Tau1 and Tau2) and weights were adjusted to provide the best fit for target EPSP and IPSP, as per existing literature (37,46). Please refer to Table 2 for the comprehensive list of parameters.

Odorant Stimulation

To stimulate the PCx network model, we used previously recorded *in vivo* spiking activity from individual mitral and tufted cells (M/Ts) as described in Dasgupta et al. (2022a). The OB activity corresponded to three different odor mixtures (A: ethyl butyrate and 2-hexanone (1:1); B: isopentyl acetate and eucalyptol (1:1); and Mix: A and B (1:1)) presented at two different frequencies (2Hz and 20Hz). Each odorant condition was simulated for 6 seconds: 2 seconds of baseline, 2 seconds of odor stimulation, and 2 seconds of post-stimulation. For each odorant condition, 336 trials were conducted, during which the synaptic connections within the PCx network model were kept constant. Synaptic inputs from M/Ts to PYRs and FFINs were randomized across trials to introduce trial-to-trial

variability. Baseline spiking in every cell of the piriform cortex generated additional trial-to-trial variability and stochasticity in the model.

Statistical Analysis

Statistical analyses were performed using MATLAB and R. To assess the network-level responses, spiking activity from all 500 pyramidal neurons (PYRs), the principal excitatory output neurons of the piriform cortex, was analysed across 336 trials for each odorant condition (odor A, odor B, and odor Mix) presented at 2Hz and 20Hz. Spike times were binned using 50ms time windows. For each trial, average firing rates were computed for individual neurons within two post-stimulus time windows (0-0.5s and 0-2s). Baseline firing rates were calculated during the -0.5 to -1.5s pre-stimulus period.

Violin plots

Two sets of comparisons were performed: (1) Odor identity comparisons (e.g., Mix vs. A, Mix vs. B, and A vs. B) at each frequency (2Hz and 20Hz); and (2) Odor frequency comparisons (2Hz vs. 20Hz) for each odor (A, B, and Mix). For odor identity comparisons, baseline-corrected firing rates of each PYR during the 0-0.5s of the stimulus period were averaged across 336 trials to generate distributions of all the PYRs for each condition. These distributions were then compared between all the odor identities in a pairwise basis. This was done for both 2Hz and 20Hz cases independently. For odor frequency comparisons, baseline-corrected firing rates were averaged across 336 trials per neuron to create distributions comparing 2Hz vs. 20Hz responses for each odor across two stimulus time windows: 0-0.5s and 0-2s. Prior to statistical testing, data distributions were assessed for normality using the Lilliefors test. As the mean firing rate distributions of all 500 PYRs significantly deviated from normality ($p < 0.05$), non-parametric Mann-Whitney (MW) U tests were performed for both comparison types. The Cliff's (47,48) delta (δ) parameter was used to quantify non-parametric effect size. This was calculated as the difference between number of instances (#) where values from Group 1 (x_{i1}) are larger than Group 2 (x_{j2}), and number of instances (#) where values from Group 1

(x_{i1}) are smaller than Group 2 (x_{j2}), divided by the product of sample sizes of Group 1 (n_1), and Group 2 (n_2), as follows:

$$\delta = \frac{\#(x_1 > x_2) - \#(x_1 < x_2)}{n1n2} \qquad (2)$$

The magnitude of effect size is assessed using the thresholds, i.e. $|\delta| < 0.147$ "negligible", $|\delta| < 0.33$ "small", $|\delta| < 0.474$ "medium", otherwise "large" (49). Cliff's δ was estimated using the "effsize" package in R. To evaluate whether odor stimulation-mediated changes in the population firing rates varied across genotypes (Control vs. Knockout) and stimulation frequencies (2Hz vs. 20Hz), a two-way mixed-design repeated measures ANOVA using the Aligned Rank Transform (ART) (50,51) procedure was implemented using the "ARTool" package in R. ART is a non-parametric procedure for properly assessing both main and interaction effects in factorial designs. The ART pre-processes the data by aligning (52,53) it and then applying mid-ranks (54) to the aligned data. The resulting aligned-and-ranked data are then analyzed using ANOVA. For these tests, genotype was a between-subject factor, whereas frequency was a within-subject factor, with neuron ID as a random effect.

Analysis of spiking data

Input resistance was calculated from the slope of the steady-state voltage response vs. subthreshold current steps graph. Action potential threshold was defined as the membrane potential (V_m) at which dV_m/dt first exceeded 20 V/s. Baseline firing rate was calculated as mean ± SD of the number of action potentials generated spontaneously per second over a duration of 1.5s in 100 trials. f-I plots were generated by quantifying the number of action potentials as a function of injected current steps over 1s for a specific cell type without noise being added. EPSP and IPSP for a specific synaptic connection were determined as the peak rise or decline in V_m from its resting membrane potential (RMP), respectively.

One-dimensional convolutional neural network (1-D CNN) model

We employed 1-D convolutional neural network (CNNs) to perform binary classification of odor stimuli based on PYRs' spiking activity (Fig. 2A). For this, spike trains were binned into non-

overlapping 20ms windows, producing binary activity vectors for each neuron based on whether a neuron spiked at least once within the specified time bin. Hence, the dimension of our dataset for any binary classification task would be $672\times100\times N$ where 672 (2×336) is the number of trials, N is the size of the PYR population used for the particular classification, and 100 is the number of time bins (2000/20). Once the dataset is prepared, it is classified into training and testing, with 60% and 40% of the data, respectively. Input to our 1-D CNN model was fed in the form of $100\times N$. In 1-D CNN, convolution is applied in 1 dimension only, which in our case is time. The convolutional layer applied temporal filters (kernel size = 3) across the input to extract time-dependent features. Convolution is a linear operation that involves multiplying the inputs with a set of weights. In our case, inputs are multiplied with the two-dimensional array of weights, known as a filter, of dimension 3×N where 3 is the kernel size. This operation assigns a unique value to each pass, resulting in a feature map with a dimension of 100. Once computed, each value in the feature map is passed to the ReLU (Rectified Linear Unit) activation function. Rectified linear unit is a linear activation function that transforms negative input to zero and outputs the same input for positive input. Convolutional neural networks may likely overfit the training data, so, a regularization technique that sets the inputs to 0 for some fraction of neurons during the training phase is used to prevent the model from overfitting. Finally, the outputs from the 1-D convolutional layer are flattened into a one dimensional vector using a flatten layer before the fully connected dense layers. These dense/fully connected layers, after application of the activation function (Softmax), map the results to the probability distribution of classes. Our 1-D CNN models consist of 2 convolution layers and 2 dense layers with a dropout rate of 0.3 applied after each layer as shown in Fig. 2A. The first convolutional layer consists of 128 filters with a kernel size of 3 along with the ReLU activation function. This layer takes the input sample in the form of 100×N and transforms the sample into 100×128. A dropout rate of 0.3 was applied after each layer to mitigate overfitting. It is then followed by another convolutional layer consisting of 128 filters with a kernel size of 3. The output from this layer is then flattened into a one dimensional vector. Finally, 2 dense layers were employed using the ReLU activation function followed by a final dense layer with the Softmax activation function for predicting the probability of the target stimulus. The model was trained using the Adam optimizer for weight optimization and categorical cross-entropy as the loss

function. During training, the number of epochs and batch size were 75 and 32, respectively. To prevent overfitting and unnecessary training, early stopping was implemented based on validation loss, with a patience parameter of 5 epochs. We conducted a series of experiments to identify the parameters that optimized the CNN's classification performance.

Logistic regression classifier

The data from all the networks were also trained and tested using Scikit-learn's SGD classifier with logistic loss function to decode odor stimulation frequencies (2Hz vs. 20Hz) for odor A, B, and Mix. As with the CNN models, these classifiers were also used to evaluate how decoding accuracy of odor-frequency classification scales with the population size of pyramidal neurons (PYRs). Data preparation for binary classification of each odor condition was identical to that used for the CNN models. For each trial, spike trains of all PYRs recorded during the 2s of odor stimulation period were divided into 100 non-overlapping time bins of 20ms each. Each time bin was assigned a value of 1 if a spike occurred within that bin for a given neuron, and 0 otherwise. This procedure resulted in a binary matrix representation of neural activity for a single trial with dimensions $100\times N$, where N denotes the number of neurons. Across trials, these matrices were stacked to form a dataset of size $672\times100\times N$ (336 trials per frequency condition).

For training and testing, the dataset was split into 60% and 40% of trials, respectively. Each trial's activity matrix was flattened into a one-dimensional feature vector of length $100\times N$, which served as input to the classifier. Prior to training, all feature vectors were standardized using Scikit-learn's StandardScaler, ensuring zero mean and unit variance. The classifier was implemented using Scikit-learn's Pipeline framework, consisting of the StandardScaler followed by an SGDClassifier configured with a logistic (log) loss function, corresponding to logistic regression classifier. The stochastic gradient descent (SGD) optimizer updated the model weights iteratively to minimize the logistic loss, offering computational efficiency and scalability for high-dimensional data. The model was trained for up to 1000 iterations with a convergence tolerance of 1×10^{-3}.

To assess how decoding accuracy scales with the PYR population size, the classifier was trained and tested on randomly sampled subsets of the PYR population. The number of neurons per subset ranged from 50 to 500 neurons, in increments of 25 neurons. For each population size, 144 independent iterations were performed with different random samples of neurons each time. The mean accuracy ± standard deviation across these iterations was then calculated. To establish a baseline for chance-level performance, a shuffle control was conducted in parallel. In this control, the class labels in the training data were randomly shuffled while keeping the feature matrices unchanged, thereby disrupting the true relationship between neural activity and stimulus frequency. The resulting shuffled accuracy thus represents chance-level decoding performance, against which the classifier's real performance was compared.

Accuracy vs. cell number

To quantify how decoding performance scales with neuronal population size, 1-D CNNs were trained and tested on PYRs subsets ranging from 50 to 500 neurons, in 50-neuron increments. For statistical robustness, 144 independent trials were conducted per population size. In each iteration, neurons were randomly sampled from the entire PYR population of 500 neurons, and data (i.e., 2×336 trials) were randomly split into training (60%) and testing (40%) sets. To establish a baseline for chance-level performance, we trained the model on datasets where the stimulus labels were randomly shuffled. This disrupted any real relationship between spiking patterns and stimulus identity while preserving the overall distribution of spike data. Decoding accuracy on the test set was recorded for each trial under both actual and shuffled-label conditions. Finally, the results were averaged across trials to compute mean accuracy and standard deviation for each population size. This analysis identified the marginal benefit of including additional neurons and helped determine whether performance plateaued at larger population sizes.

Determining cell importance

The importance of individual neurons for binary classification was quantified using negative cross-entropy loss (log-likelihood) of the CNN model. Log-likelihood measures how well the model's

probability predictions align with the true class labels (1 or 0). Mathematically, it is calculated as the sum of log predicted probabilities of true class labels in the test set. Higher values of log-likelihood indicate better model performance, meaning stronger alignment between predictions and actual class labels. The odor frequency trials of PYRs were randomly divided into two sets: a training set (70%) and a test set (30%). The CNN models were trained and tested on the data corresponding to odor stimulation period (i.e., 2-4s) and then log-likelihood was calculated. Then we replaced a given neuron's stimulus response activity with its baseline/pre-stimulus activity in the test set and again calculated the log-likelihood. The impact of this perturbation was measured by the difference between log-likelihood of the model for intact and perturbed conditions (ΔLL). A substantial reduction indicated that the neuron was critical for decoding. We performed this analysis for all 500 PYRs one at a time. Neuron importance score was defined as the mean of ΔLL across all 300 iterations, with higher values indicating greater contribution to stimulus discrimination. Finally, neurons were ranked by their mean importance scores, revealing their relative importance to the model's performance. This procedure was performed separately for each experimental condition (A, B, and Mix). CNN architecture for this analysis was largely the same as outlined above except the number of epochs during training was 15 to avoid overfitting.

Accuracy using baseline firing data

To evaluate the model's behavior in the absence of stimulus, we trained and tested the model exclusively on baseline firing data (0–2s) of all 500 PYRs using the same CNN architecture and method outlined above. This experiment-tested whether the model learned any spurious patterns not directly related to the stimulus (Fig. S5). A total of 144 iterations were conducted, with each iteration involving a random 60%/40% train-test split.

PYRs population baseline firing rate

Spike data from all 500 pyramidal neurons were binned into 2s time windows and converted to firing rates (Hz) for all six odor conditions across 336 trials. Population baseline firing rates across all network conditions were calculated by averaging the firing rate during the first time bin (0–2s, i.e.,

the baseline period) across all neurons, trials, and odor conditions. Data were analyzed using custom MATLAB functions, with mean ± standard deviation computed across all network conditions.

Code Accessibility

The NEURON simulation codes are available at https://github.com/ankitbishnoe29/Piriform-Cortex-network-Project.git

Results

To investigate if the odor frequency is encoded in the piriform cortex (PCx), we constructed a biophysically relevant network model comprising 500 pyramidal neurons (PYRs), 50 feedforward interneurons (FFINs), and 50 feedback interneurons (FBINs) (Fig. 1A). The model's architecture and connection probabilities were based on experimental data from rodents (45,54,55) as described in the methods section as described in the materials and methods section. Previously recorded activity from M/T cells *in vivo* as described in Dasgupta et al. (2022) were used as the olfactory bulb (OB) output which formed the PCx model input. The OB activity was in response to three different odor mixtures (A: ethyl butyrate and 2-hexanone (1:1); B: isopentyl acetate and eucalyptol (1:1); Mix: A and B (1:1)) presented at two frequencies (2Hz and 20Hz). The model was simulated using the NEURON environment for 6s (2s baseline followed by 2s of odor stimulation and 2s of post-stimulation).

Each PYR was modeled to have a soma connected to an apical dendritic trunk made of five dendritic sections (Fig. S1A). The FFINs and FBINs were modelled to have just a single somatic compartment (Fig. S1B-C). The resting membrane potentials of PYRs, FFINs, and FBINs were -74.1 ± 8.6 mV, -72 ± 5.9 mV, and -77.8 ± 11.3 mV, respectively. This corroborated previous experimental findings (40,43). The PYRs, FFINs and FBINs (Fig. S2E; Fig. S3D; Fig. S4D) showed similar action potential firing profiles compared to experimentally observed recordings (41,43). The spontaneous baseline firing rate calculated from the soma of PYR, FFIN, and FBIN was 2.22 ± 0.98 Hz (Fig. S2D), 2 ± 1.14 Hz (Fig. S3F), and 6.55 ± 2.11 Hz (Fig. S4F), respectively (58). The estimated input resistance values measured from the soma and the dendrites of PYRs (79.84, 80.28, 84.94, 99.36, 137.58, and 246.18 MΩ from the soma and dend1 to dend5, respectively) (Fig. S2B) were consistent

with experimental findings (40). The input resistance measured from the FFINs and the FBINs was 93.36 MΩ (Fig. S3B(III)) and 50.29 MΩ (Fig. S4B(III)), respectively (43). We recorded spike timings of all 500 PYRs across 336 trials for each odor stimulation condition. Spike trains from individual trials were converted into firing rates within two post-stimulus windows: the initial 0-0.5s and the entire 0-2s of the odor stimulation period. The firing rates were baseline-corrected on a trial-by-trial basis for all the PYRs across all the odor conditions.

Pyramidal neurons of the PCx can discriminate odor identity largely irrespective of the odor frequency

Overall, we had six odor stimulation conditions: Odor A, Odor B, and Odor Mix each presented at 2Hz and 20Hz. To investigate whether the PYR population activity could help discriminate the odor identities, firing rate distributions corresponding to the initial 0–0.5s window were compared between different odor pairs for the 2Hz and the 20Hz cases independently (Fig. 1C-E). The PYR population response to odor Mix and odor A at 2Hz showed non-significant difference (Mix: 0.37Hz, IQR = 0.30 - 0.45Hz, n = 500, and A: 0.37Hz, IQR = 0.31 - 0.44Hz, n = 500; Mann-Whitney p = 0.952; Cliff's |δ| = 0.002, "negligible" effect size; Fig. 1C). In contrast, for the 20Hz case, we observed a significant difference between the firing rate distribution (Mix: 0.41Hz, IQR = 0.33 - 0.47Hz; A: 0.48Hz, IQR = 0.41 - 0.56Hz; Mann-Whitney p = 7.01e-27; Cliff's |δ| = 0.392, "medium" effect size; Fig. 1C). For the Mix vs. B, PYRs exhibited small but significant differences in the population-level firing for the 2Hz case (Mix: 0.37Hz, IQR = 0.30 - 0.45Hz, n = 500; B: 0.43Hz, IQR = 0.36 - 0.50Hz, n = 500; Mann-Whitney p = 2.94e-13; Cliff's |δ| = 0.267, "small" effect size; Fig. 1D). For the 20Hz case, firing rates of the PYR population were significantly higher for odor Mix than for odor B (Mix: 0.41Hz, IQR = 0.33 - 0.47Hz; B: 0.32Hz, IQR = 0.25 - 0.39Hz, n = 500; Mann-Whitney p = 5.45e-30; Cliff's δ = 0.416, "medium" effect size; Fig. 1D). The responses to odors A and B differed modestly but significantly at 2 Hz (A: 0.37Hz, IQR = 0.31 - 0.44Hz; B: 0.43Hz, IQR = 0.36 - 0.50Hz, n = 500; Mann-Whitney p = 1.89e-14; Cliff's |δ| = 0.28, "small" effect size; Fig. 1E). However, at 20Hz, PYRs fired more strongly for odor A than for odor B (A: 0.48Hz, IQR = 0.41 -

0.56Hz; B: 0.32Hz, IQR = 0.25 - 0.39Hz, n = 500; Mann-Whitney p = 1.48e-83; Cliff's δ = 0.708, "large" effect size; Fig. 1E).

Overall, these results demonstrate that the piriform cortex model can discriminate between identities of complex odor mixtures largely for both 2Hz as well as 20Hz odor frequencies. However, odor identity discrimination was weaker ("*negligible*" to "*small*" effect sizes) at 2Hz compared to the 20Hz cases ("*medium*" to "*large*" effect sizes).

The Piriform Cortex model can discriminate 2Hz from 20Hz odor frequency

Next, we examined whether the piriform cortex responds differently to the 2Hz and 20Hz stimulation frequencies of the same odor. For this, PYRs responses were quantified during two post-stimulus windows: the initial 0–0.5s and the entire 0–2s odor stimulation period over 336 trials. The 0.5s window was chosen to justify the decision-making time based on previously observed behavioral assays (19). For each odor, baseline-corrected mean firing rate distributions for the entire PYR population were compared between 2Hz and 20Hz stimulation for each time window (Fig. 1F–H).

For odor A, during the 0-0.5s window, the PYR population exhibited a significant increase in median firing rate from 0.37Hz (IQR = 0.31 - 0.44Hz) at 2Hz stimulation to 0.48Hz (IQR = 0.41 - 0.56Hz) at 20Hz stimulation (n = 500; Mann-Whitney p = 2.2e-48; Cliff's δ = -0.534, "large" effect size; Fig. 1F). During the 0-2s window, median firing rate increased from 0.47Hz (IQR = 0.42 - 0.52Hz) at 2Hz to 0.53Hz (IQR = 0.48 - 0.57Hz) at 20Hz (n = 500; Mann-Whitney p = 2.16e-28; Cliff's δ = -0.404, "medium" effect size; Fig. 1F). For odor B, during the 0-0.5s window, PYRs median firing rate decreased significantly from 0.43Hz (IQR = 0.36 - 0.5Hz) at 2Hz to 0.32Hz (IQR = 0.25 - 0.39Hz) at 20Hz (n = 500; Mann-Whitney p = 1.23e-44; Cliff's δ = 0.512, "large" effect size; Fig. 1G). Similarly, during the 0-2s window, the median firing rate also decreased significantly from 0.44Hz (IQR = 0.4 - 0.49Hz) at 2Hz to 0.34Hz (IQR = 0.29 - 0.39Hz) at 20Hz (n = 500; Mann-Whitney p = 2.53e-85; Cliff's δ = 0.715, "large" effect size; Fig. 1G). For odor Mix, PYRs showed a small but significant increase in firing rate during the initial 0-0.5s window, from a median of 0.37Hz (IQR = 0.30–0.45 Hz) at 2Hz to 0.41Hz (IQR = 0.33–0.47 Hz) at 20Hz (n = 500; Mann-Whitney p = 2.7e-05; Cliff's δ = –0.153, "small" effect size; Fig. 1H). However, during the 0–2s window, firing rates slightly

decreased from 0.49Hz (IQR = 0.44–0.53 Hz) at 2Hz to 0.45Hz (IQR = 0.41–0.51 Hz) at 20Hz (Mann-Whitney p = 1.74e-10; Cliff's δ = 0.233, "small" effect size; Fig. 1H).

These findings indicate that irrespective of odor identities, PYR population can discriminate between 2Hz and 20Hz odor frequency.

However, it is important to understand whether individual neurons can also discriminate odor frequencies. To understand this, we next analysed the activities of all the PYRs individually. We used the same time windows and trials for the analysis as before and compared them using a two-tailed Mann–Whitney U test (n = 336). Neurons exhibiting significant differences ($p < 0.05$) were classified as odor frequency–discriminating cells, and effect sizes were estimated using Cliff's |δ|. For odor A, during the 0-0.5s window, 53 out of 500 neurons were frequency-discriminating, with 51 and 2 of them showing "negligible" and "small" effect sizes respectively (Fig. 1I). For the 0-2s window, 51 out of 500 neurons were frequency-discriminating, with 50 and 1 showing "negligible" and "small" effect size respectively (Fig. 1I). For odor B, during the 0-0.5s window, 65 of 500 neurons were frequency-discriminating, of which 63 and 2 cells showed "negligible" and "small" effect sizes respectively (Fig. 1J). For the 0-2s window, out of the 106 frequency-discriminating neurons, 101 and 5 showed "negligible" and "small" effect sizes respectively (Fig. 1J). For the odor Mix, 26 of 500 neurons were frequency-discriminating during the 0-0.5s window, with 25 and 1 showing "negligible" and "small" effect sizes, respectively, while for the 0-2s window, out of 32 frequency-discriminating cells, 30 and 2 cells showed "negligible" and "small" effect sizes respectively (Fig. 1K).

However, given the multiple comparisons involved in testing 500 individual neurons, we applied a Bonferroni correction. Under this conservative criterion ($p < 0.05/500$), no frequency-discriminating cells were identified for odor A and B in either time window. For odor Mix, only a single neuron showed significant discrimination during the 0-2s window with a "small" effect size, while no discriminating neurons were found in the 0-0.5 window.

Collectively, these findings suggest that spike count responses of individual PYRs are insufficient to reliably distinguish odor frequencies while the overall PYR population firing rate

shows better discrimination of odor frequencies for all the different odor mixtures. This raises the possibility that odor frequency discrimination likely emerges at the population level through coordinated activity across neurons.

To examine how accurately odor frequency could be decoded from the population activity in the PCx network model, we quantified PYRs responses as binary spike vectors (1s and 0s) over the entire 2s odor stimulation period. Each trial was divided into 20ms non-overlapping time bins, where a value of 1 indicated at least one spike within that bin. 60% of the activity matrices for 2Hz and 20Hz odor trials were then used to train one-dimensional convolutional neural network (1D-CNN) models which were then tested on the remaining 40% of the trial data (Fig. 2A).

The CNN models achieved final peak decoding accuracies of 0.95 ± 0.016, 0.87 ± 0.032, and 0.73 ± 0.043 (mean ± SD) for distinguishing 2Hz from 20Hz odor stimulation for odors A, B, and Mix, respectively. In contrast, the shuffled controls yielded chance-level peak accuracies of 0.51 ± 0.025, 0.5 ± 0.027, 0.51 ± 0.028 for odors A, B, and Mix, respectively. We also evaluated how decoding accuracy scaled with population size by training and testing CNN models on randomly selected subsets of PYRs of increasing sizes (Fig. 2B). Each subset size was evaluated over 144 independent iterations. The classification accuracy increased monotonically with increase in the number of neurons included while consistently outperformed shuffled controls across all the different odors. To ensure that the CNN models did not suffer from any intrinsic bias, additional CNN models were trained and tested on the baseline activity of PYRs in a similar way (Fig. S5), which showed no significant deviation from their corresponding shuffle controls.

We next quantified the relative contribution of individual pyramidal neurons to the odor frequency decoding accuracy in the CNN models. To do this, in the test set we systematically replaced a given neuron's odor period activity with its baseline activity one-at-a-time, and recalculated the log-likelihood. For each neuron's perturbation, we computed the mean change in log-likelihood (ΔLL; intact minus perturbed) across 300 independent iterations and ranked neurons in descending order of ΔLL (Fig. 2C). Larger positive ΔLL values indicated greater contribution to odor frequency discrimination, whereas near-zero or negative values reflected minimal or adverse contributions. We

observed that the ΔLL values for all three odors are distributed along a continuum. Neurons on the left extreme contribute positively, those on the right extreme contribute negatively, and those in between contribute equally and minimally. Together, these findings suggest that the odor-frequency discrimination capacity is distributed among the entire PYR population.

To validate the findings of non-linear models (CNN) using linear models, we also trained and tested logistic regression classifiers to decode odor stimulation frequencies for each odor condition (odor A, B, and Mix; Fig. 2D). Data preparation for this linear classifier was identical to that used for the CNN models, except that the input was formatted as one-dimensional feature vectors of length 100 × N, where 100 represents the number of 20ms time bins, and N is the number of neurons. The logistic regression classifiers achieved mean peak accuracies of 0.89 ± 0.015, 0.84 ± 0.019, and 0.70 ± 0.022 for odor A, B, and Mix, respectively. Similar to the CNN models, decoding accuracy of the logistic regression models increased monotonically with population size (Fig. 2D) and closely resembled the performance of CNN models (Fig. 2B, D).

Together, these results indicate that the spiking patterns of PYRs carry crucial information for odor frequency discrimination. Furthermore, we have observed that both non-linear (CNN) as well as linear (logistic regression) decoders can capture this information, suggesting that odor frequency encoding is a network-level phenomenon with a distributed role of PYRs.

Different synaptic connections differentially affect odor frequency discrimination

Given that frequency coupling with membrane potential of the M/T cells has been observed to be influenced by the local inhibition in the olfactory bulb (19), we next investigated how different types of synaptic connections might be playing a role in influencing frequency discrimination in the PCx model. We systematically removed each synaptic connection type from the control network model, one at a time, and assessed its effect on odor-frequency discrimination performance. For each knockout condition, the PCx knockout models were simulated in a similar way as for the control case, and the PYRs' spiking activities were examined in the same manner as before.

Eliminating either feedforward or feedback inhibition enhanced odor frequency discrimination

To investigate the influence of direct inhibitory inputs onto the PYRs in the context of odor frequency discrimination, we selectively removed the synaptic connections from feedforward (FF), and feedback (FB) interneurons onto the PYRs one at a time (Fig. 3A; Fig. 4A). We then trained 1-D CNN models as before to classify 2Hz vs. 20Hz odor trials based on PYR population activity. Both knockout models yielded higher decoding accuracy compared with the Control network across all population sizes (Fig. 3B; Fig. 4B; Fig. S6).

For the FF-PYR knockout model, CNNs achieved peak decoding accuracies (mean ± SD, N = 500 neurons) of 0.98 ± 0.006, 0.96 ± 0.011, and 0.87 ± 0.03 for odor A, B and Mix respectively (Fig. 3B). Logistic regression classifiers trained on the same activity achieved peak accuracies of 0.97 ± 0.01, 0.94 ± 0.015, and 0.81 ± 0.019, respectively (Fig. S6). Similarly, for the FB-PYR knockout model, CNNs achieved peak accuracies of 0.99 ± 0.005 for odor A, 0.97 ± 0.011 for odor B, and 0.88 ± 0.02 for Mix (Fig. 4B). Logistic regression classifiers again produced comparable peak accuracies of 0.98 ± 0.007, 0.97 ± 0.009, and 0.88 ± 0.02, respectively (Fig. S6).

We also analyzed the odor-frequency discrimination using averaged spiking activity-based analysis as for the control case.

For odor A, during the 0-0.5s post-stimulus window, the median firing rate of PYRs increased from 0.53Hz (IQR = 0.44 - 0.60Hz) at 2Hz stimulation to 0.70Hz (IQR = 0.63 - 0.78Hz) at 20 Hz stimulation (Mann-Whitney p = 4.34e-89; Cliff's |δ| = 0.731, "large" effect size; Fig. 3C, left). We compared the results with the control case as well. Mixed two-way repeated-measures ART-ANOVA revealed significant main effects of genotype (p = 2.93e-202) and frequency (p = 3.77e-143), as well as a genotype × frequency interaction (p = 4.93e-13). A significant genotype × frequency interaction indicates that the two genotypes differ statistically in their degree of change in firing rates across stimulation frequencies. The magnitude of this change is reflected by Cliff's |δ|, which quantifies the degree of distributional non-overlap between two distributions (48,59). Thus, a genotype demonstrates statistically stronger frequency discrimination when it exhibits a higher Cliff's |δ| relative to the other along with a significant genotype × frequency interaction.

During the 0-2s post-stimulus window, the median firing rate increased from 0.66Hz (IQR = 0.61 - 0.72Hz) at 2Hz to 0.78Hz (IQR = 0.73 - 0.84Hz) at 20Hz (Mann-Whitney p = 9.67e-87; Cliff's |δ| =

0.721, “large” effect size; Fig. 3C, right). The ART-ANOVA analysis with the corresponding control case again revealed significant main effects of genotype ($p < 2.225e-308$), frequency ($p = 6.79e-116$), and genotype × frequency interaction ($p = 1.65e-20$). Please refer to Table 3 to see the complete summary of the p values for the main and interaction effects.

Based on this criterion, FF-PYR knockout mice exhibited enhanced odor-frequency discrimination for odor A across both time windows compared to control.

For odor B, during 0-0.5s post-stimulus window, the median firing rate decreased from 0.62Hz (IQR = 0.53 - 0.70Hz) at 2Hz to 0.48Hz (IQR = 0.41 - 0.56Hz) at 20Hz (Mann-Whitney $p = 2.09e-53$; Cliff’s $|\delta| = 0.562$, “large” effect size; Fig. 3D, left). Comparing it with the control, ART-ANOVA revealed significant main effects of genotype ($p = 7.48e-178$), frequency ($p = 1.58e-100$), and a modest genotype × frequency interaction ($p = 0.007$). During 0-2s post stimulation window, the median firing rate decreased from 0.64Hz (IQR = 0.59 - 0.69Hz) at 2Hz to 0.5Hz (IQR = 0.45 - 0.55Hz) at 20Hz (Mann-Whitney $p = 7.72e-111$; Cliff’s $|\delta| = 0.817$, “large” effect size; Fig. 3D, right). Comparing it with the control, ART-ANOVA again indicated significant main effects of genotype ($p = 1.07e-321$), frequency ($p = 2.05e-210$), as well as genotype × frequency interaction ($p = 3.08e-08$). These results also supported increased odor-frequency discrimination for odor B in FF-PYR knockout compared to control.

For odor Mix, during the 0-0.5s post-stimulus window, median firing rate of PYRs increased modestly from 0.53Hz (IQR = 0.45 - 0.61Hz) at 2Hz to 0.58Hz (IQR = 0.50 - 0.66Hz) at 20Hz (Mann-Whitney $p = 5.45e-10$; Cliff’s $|\delta| = 0.227$, “small” effect size; Fig. 3E, left), Comparing it with the control, ART-ANOVA revealed significant main effects of genotype ($p = 5.45e-164$), frequency ($p = 3.84e-14$), but without genotype × frequency interaction ($p = 0.063$). However, during 0-2s post-stimulus window, the median firing rate decreased from 0.71Hz (IQR = 0.66 - 0.76Hz) at 2Hz to 0.66Hz (IQR = 0.61 - 0.71Hz) at 20Hz (Mann-Whitney $p = 4.98e-19$; Cliff’s $|\delta| = 0.326$, “small” effect size; Fig. 3E, right). Comparing it with the control, ART-ANOVA indicated significant effects of genotype ($p < 2.225e-308$), frequency ($p = 6.36e-28$), and a genotype × frequency interaction ($p = 0.034$). These findings indicate enhanced odor-frequency discrimination in FF-PYR knockout relative to control for odor Mix only during the entire 0-2s window of odor stimulation.

Overall, based on the statistical tests, the CNNs and the logistic regression classifiers, FF-PYR knockout model exhibited robust discrimination between 2Hz and 20Hz stimulation frequencies relative to control across all odors and largely across both the analysis windows.

Next, we assessed the odor-frequency discrimination in FB-PYR model. For odor A, the FB-PYR knockout model exhibited stronger discrimination between stimulation frequencies relative to control across both post-stimulation time windows. During the 0-0.5s post-stimulus window, median firing rates in the knockout model increased from 0.73Hz (IQR: 0.64 - 0.82Hz) at 2Hz to 0.97Hz (IQR: 0.88 – 1.08Hz) at 20Hz (Mann-Whitney p = 4.87e-101; Cliff's |δ| = 0.78, "large" effect size; Fig. 4C, left). Comparing it with the control, ART-ANOVA revealed significant main effects of genotype (p < 2.225e-308) and frequency (p = 1.55e-169), as well as a genotype × frequency interaction (p = 5.72e-32). During the 0-2s window, median firing rates increased from 0.95Hz (IQR: 0.88 – 1.02Hz) at 2Hz to 1.10Hz (IQR: 1.03 – 1.17Hz) at 20Hz (Mann-Whitney p = 9.5e-90; Cliff's |δ| = 0.734, "large" effect size; Fig. 4C, right). Comparing it with control, ART-ANOVA revealed significant main effects of genotype (p < 2.225e-308) and frequency (p = 1.44e-127), as well as a genotype × frequency interaction (p = 4.84e-37).

In case of odor B, the FB-PYR knockout model also exhibited greater frequency discrimination relative to control across both post-stimulation time windows. During the 0-0.5s post-stimulus window, median firing rates decreased from 0.87Hz (IQR: 0.78 - 0.97Hz) at 2Hz to 0.67Hz (IQR: 0.57 – 0.76Hz) at 20Hz (Mann-Whitney p = 1.54e-81; Cliff's |δ| = 0.699, "large" effect size; Fig. 4D, left). Comparing it with control, ART-ANOVA revealed significant main effects of genotype (p < 2.225e-308) and frequency (p = 1.68e-134), as well as a genotype × frequency interaction (p = 7.02e-20). During the 0-2s post-stimulus window, median firing rates decreased from 0.91Hz (IQR: 0.84 – 0.97Hz) at 2Hz to 0.68Hz (IQR: 0.62 – 0.75Hz) at 20Hz (Mann-Whitney p = 2.64e-134; Cliff's |δ| = 0.901, "large" effect size; Fig. 4D, right). Comparing with control, ART-ANOVA revealed significant main effects of genotype (p < 2.225e-308) and frequency (p = 2.96e-257), as well as a genotype × frequency interaction (p = 2.04e-50).

For odor Mix, both the FB-PYR knockout and control models showed limited and comparable discrimination between stimulation frequencies during the 0-0.5s post-stimulus window. Median

firing rates in the knockout model increased slightly from 0.77Hz (IQR: 0.68 - 0.87Hz) at 2Hz stimulation to 0.81Hz (IQR: 0.71 – 0.90Hz) at 20Hz stimulation (Mann-Whitney p = 0.00026; Cliff's |δ| = 0.133, "negligible" effect size; Fig. 4E, left). Comparing with control, ART-ANOVA revealed significant main effects of genotype (p < 2.225e-308), frequency (p = 1.5e-08), but no genotype × frequency interaction (p = 0.696).

However, during the 0-2s post-stimulus window, median firing rates in the knockout model decreased from 1.01Hz (IQR: 0.95 – 1.08Hz) at 2Hz stimulation to 0.93Hz (IQR: 0.86 – 1Hz) at 20Hz stimulation (Mann-Whitney p = 3.43e-35; Cliff's |δ| = 0.452, "medium" effect size; Fig. 4E, right). Comparing it with control, ART-ANOVA revealed significant main effects of genotype (p < 2.225e-308) and frequency (p = 8.85e-45), as well as a genotype × frequency interaction (p = 4.72e-11).

These findings are in line with the observations from linear and non-linear models that both without FF-PYR and FB-PYR knockouts models exhibited enhanced odor-frequency discrimination for all three odor mixtures, taking the entire 2s odor stimulation period into consideration.

Eliminating intra-inhibitory connections singularly had minimal effect on odor frequency discrimination

The PCx network contains a substantial amount of intra-inhibitory connections among feedforward (FF) as well as feedback (FB) interneurons (46). To understand the influence of these disinhibitory motifs on odor frequency discrimination, we eliminated the synaptic intra-connections among FF and FB interneurons individually in two distinct knockout models (Fig. 5A, 6A). Both knockout models demonstrated comparable decoding accuracy to the control network across various population sizes (Fig. 5B; Fig. 6B; Fig. S6). Peak accuracy achieved by CNNs for FF-FF knockout model was 0.92 ± 0.016 (odor A), 0.87 ± 0.023 (odor B), and 0.7 ± 0.05 (odor Mix), whereas for FB-FB knockout model accuracy was 0.93 ± 0.015 (odor A), 0.87 ± 0.028 (odor B), and 0.73 ± 0.04 (odor Mix) (Fig. 5B, 6B). Logistic regression classifiers achieved peak decoding accuracies of 0.85 ± 0.019, 0.82 ± 0.018, and 0.68 ± 0.023 for odors A, B, and Mix, respectively, in the FF-FF knockout model and 0.86 ± 0.019, 0.82 ± 0.02, and 0.71 ± 0.025 for the same odor pairs in the FB-FB knockout model (Fig. S6).

For odor A, frequency discrimination in the FF-FF knockout model was comparable to that of the control when responses were analyzed during either the initial 0-0.5s or entire 0-2s window of

odor stimulation (Fig. 5C). During the initial 0-0.5s window, the median firing rate of PYRs increased from 0.32Hz (IQR: 0.25 - 0.38Hz) at 2Hz stimulation to 0.41Hz (IQR: 0.35 - 0.48Hz) at 20Hz stimulation (Mann-Whitney p = 1.33e-46; Cliff's |δ| = 0.524, "large" effect size; Fig. 5C, left). Relative to control, ART-ANOVA showed significant main effects of genotype (p = 8.33e-38) and frequency (p = 8.89e-96), with no genotype × frequency interaction (p = 0.2475). During the 0-2s window, the median firing rate increased from 0.40Hz (IQR: 0.36 - 0.45Hz) at 2Hz stimulation to 0.46Hz (IQR: 0.41 – 0.51Hz) at 20Hz stimulation (Mann-Whitney p = 1.29e-34; Cliff's |δ| = 0.448, "medium" effect size; Fig. 5C, right). ART-ANOVA again showed significant main effects of genotype (p = 3.55e-80) and frequency (p = 3.05e-62), with no genotype × frequency interaction (p = 0.2997).

For odor B, frequency discrimination remained comparable to control during the 0-0.5s window. Here PYRs' median firing rate decreased from 0.38Hz (IQR: 0.30 – 0.45Hz) at 2Hz stimulation to 0.28Hz (IQR: 0.22-0.35Hz) at 20Hz stimulation (Mann-Whitney p = 1.68e-41; Cliff's |δ| = 0.493, "large" effect size; Fig. 5D, left). ART-ANOVA revealed significant main effects of genotype (p = 9.46e-22) and frequency (p = 3.19e-88), with no genotype × frequency interaction (p = 0.2354). During the 0-2s window, PYRs' median firing rate decreased from 0.39Hz (IQR: 0.34 – 0.43Hz) at 2Hz stimulation to 0.30Hz (IQR: 0.25 - 0.34Hz) at 20Hz stimulation (Mann-Whitney p = 6.57e-77; Cliff's |δ| = 0.678, "large" effect size; Fig. 5D, right). However, for this time window, ART-ANOVA revealed a significant genotype × frequency interaction (p = 0.0468), alongside significant main effects of genotype (p = 4.45e-53) and frequency (p = 3.39e-168), indicating slightly higher discrimination in control.

For the odor Mix, frequency discrimination in the knockout model remained comparable to control for both time windows (Fig. 5E). During the 0-0.5s window, the median firing rate of PYRs increased slightly from 0.32Hz (IQR: 0.25 - 0.40Hz) at 2Hz stimulation to 0.35Hz (IQR: 0.29 - 0.42Hz) at 20Hz stimulation (Mann-Whitney p = 1.49e-05; Cliff's |δ| = 0.158, "small" effect size; Fig. 5E, left). ART-ANOVA showed significant main effects of genotype (p = 3.72e-24) and frequency (p = 1.1e-09), with no genotype × frequency interaction (p = 0.9345). During the 0-2s window, the median firing rate decreased from 0.42Hz (IQR: 0.38 - 0.47Hz) at 2Hz stimulation to 0.39Hz (IQR: 0.35 – 0.44Hz)

at 20Hz stimulation (Mann-Whitney p = 4.5e-12; Cliff's |δ| = 0.253, "small" effect size; Fig. 5E, right). ART-ANOVA again revealed significant main effects of genotype (p = 1.51e-77) and frequency (p = 6.39e-21) without a genotype × frequency interaction (p = 0.9085).

Next, the control and without FB-FB knockout models both exhibited comparable odor frequency discrimination for odor A and Mix. However, for odor B, the knockout model showed reduced discrimination ability compared to control across both time stimulus windows (Fig. 6C-E).

For odor A, during the 0-0.5s window, median PYRs firing rate increased substantially from 0.33Hz (IQR: 0.25 - 0.39Hz) at 2Hz stimulation to 0.43Hz (IQR: 0.36 - 0.50Hz) at 20Hz stimulation (Mann-Whitney p = 4.93e-50; Cliff's |δ| = 0.543, "large" effect size; Fig. 6C, left). ART-ANOVA showed significant main effects of genotype (p = 5.44e-26) and frequency (p = 1.32e-99), with no genotype × frequency interaction (p = 0.9515). During the 0-2s window, median firing rate increased from 0.42Hz (IQR: 0.37 - 0.46Hz) at 2Hz stimulation to 0.48Hz (IQR: 0.43 – 0.53Hz) at 20Hz stimulation (Mann-Whitney p = 4.58e-43; Cliff's |δ| = 0.503, "large" effect size; Fig. 6C, right). ART-ANOVA again revealed significant main effects of genotype (p = 6.79e-49) and frequency (p = 2.92e-69) without a genotype × frequency interaction (p = 0.0668).

For odor B, during the 0-0.5s window, PYRs' median firing rate decreased from 0.37Hz (IQR: 0.32 – 0.45Hz) at 2Hz stimulation to 0.29Hz (IQR: 0.23 - 0.36Hz) at 20Hz stimulation (Mann-Whitney p = 4.67e-32; Cliff's |δ| = 0.431, "medium" effect size; Fig. 6D, left). The higher Cliff's |δ| in control relative to knockout, along with significant main effects of genotype (p = 2.31e-15), frequency (p = 1.32e-75), and a genotype × frequency interaction (p = 0.0169) by ART-ANOVA indicated better discrimination in control. During the 0-2s window, PYRs' median firing rate decreased markedly from 0.40Hz (IQR: 0.35 – 0.45Hz) at 2Hz stimulation to 0.31Hz (IQR: 0.26 - 0.35Hz) at 20Hz stimulation (Mann-Whitney p = 9.17e-75; Cliff's |δ| = 0.668, "large" effect size; Fig. 6D, right). The lower Cliff's |δ| in knockout relative to control along with significant main effects of genotype (p = 2.05e-31), frequency (p = 3.25e-166), and a genotype × frequency interaction (p = 0.0327), confirmed slightly impaired discrimination in knockout.

For the odor Mix, frequency discrimination in the knockout model remained comparable to control across both time windows (Fig. 6E). During the 0-0.5s window, the median firing rate of PYRs

increased modestly from 0.32Hz (IQR: 0.26 - 0.40Hz) at 2Hz stimulation to 0.37Hz (IQR: 0.30 - 0.44Hz) at 20Hz stimulation (Mann-Whitney p = 3.67e-10; Cliff's |δ| = 0.229, "small" effect size; Fig. 6E, left). ART-ANOVA showed significant main effects of genotype (p = 3.88e-19) and frequency (p = 6.46e-14), with no genotype × frequency interaction (p = 0.1883). During the 0-2s window, the median firing rate showed a minimal decrease from 0.43Hz (IQR: 0.39 - 0.48Hz) at 2Hz stimulation to 0.42Hz (IQR: 0.37 – 0.46Hz) at 20Hz stimulation (Mann-Whitney p = 1.78e-06; Cliff's |δ| = 0.174, "small" effect size; Fig. 6E, right). ART-ANOVA again revealed significant main effects of genotype (p = 1.24e-41) and frequency (p = 1.52e-15) without a genotype × frequency interaction (p = 0.1445).

Overall, our results demonstrate that eliminating the intra-inhibitory connections within either feedforward or feedback inhibitory interneuron populations did not substantially affect odor frequency discrimination.

Eliminating either excitatory or all intra-inhibitory recurrent connections impaired odor frequency discrimination

Finally, to investigate how removing recurrent inhibition in both interneuron types simultaneously affects frequency encoding in the PCx model, we developed a model that exhibited both FF-FF and FB-FB knockout simultaneously (Fig. 7A). To investigate the same effect by removing recurrent excitation onto PYRs, we developed a without PYR-PYR knockout model (Fig. 8A). Decoding of odor frequency responses using 1-D CNN models revealed a decline in classification accuracy for both knockout models across all size-matched populations of PYRs compared to the control (Fig. 7B, 8B). The peak accuracies achieved in the without FF-FF and FB-FB knockout model were A: 0.91 ± 0.02; B: 0.83 ± 0.029; and Mix: 0.67 ± 0.05 (Fig. 7B). The peak accuracies achieved in the without PYR-PYR knockout model were A: 0.92 ± 0.02; B: 0.84 ± 0.03; and Mix: 0.69 ± 0.05 (Fig. 8B) compared to the control (A: 0.95 ± 0.016; B: 0.87 ± 0.032; and Mix: 0.73 ± 0.043).

Logistic regression classifier also displayed similar impairments in decoding accuracies (Fig. S6). The peak decoding accuracies achieved using the responses of FF-FF and FB-FB knockout model were A: 0.85 ± 0.02; B: 0.78 ± 0.021; and Mix: 0.64 ± 0.026, whereas those from the PYR-PYR knockout model were A: 0.82 ± 0.017; B: 0.79 ± 0.02; and Mix: 0.66 ± 0.023 (Fig. S6).

The FF-FF and FB-FB knockout model demonstrated impaired odor-frequency discrimination compared with the control group for odor A and Mix during the 0-0.5s stimulus window, and for odor B, even during the 0-2s window.

For odor A, during the 0-0.5s post-stimulus window, PYRs' median firing rate in the knockout model increased from 0.30Hz (IQR: 0.23 – 0.36Hz) at 2Hz to 0.37Hz (IQR: 0.31 – 0.44Hz) at 20Hz (Mann-Whitney p = 7.83e-31; Cliff's |δ| = 0.422, "medium" effect size; Fig. 7C, left). Compared with the control (Cliff's |δ| = 0.534), ART-ANOVA revealed significant main effects of genotype (p = 3.06e-80) and frequency (p = 8.69e-78), as well as a genotype × frequency interaction (p = 0.0011), indicating impaired frequency discrimination in knockout model. During the 0-2s window, median firing rate increased from 0.37Hz (IQR: 0.32 – 0.42Hz) at 2Hz to 0.42Hz (IQR: 0.37 – 0.47Hz) at 20Hz (Mann-Whitney p = 9.57e-25; Cliff's |δ| = 0.375, "medium" effect size; Fig. 7C, right). Comparing it with control, ART-ANOVA revealed significant main effects of genotype (p = 3.12e-161) and frequency (p = 1.81e-51) but no genotype × frequency interaction (p = 0.4955), suggesting comparable discrimination between control and knockout.

For odor B, during the 0-0.5s window, median firing rate decreased from 0.34Hz (IQR: 0.27 – 0.42Hz) at 2Hz stimulation to 0.27Hz (IQR: 0.21 – 0.35Hz) at 20Hz stimulation (Mann-Whitney p = 2.93e-21; Cliff's |δ| = 0.346, "medium" effect size; Fig. 7D, left). The larger effect size observed in control (Cliff's |δ| = 0.512) relative to knockout, along with significant main effects of genotype (p = 1.53e-41), frequency (p = 1.66e-64), and a genotype × frequency interaction (p = 3.85e-05) by ART-ANOVA, indicated superior discrimination in control. During the 0-2s window, PYRs median firing rate decreased markedly from 0.36Hz (IQR: 0.31 – 0.41Hz) at 2Hz stimulation to 0.28Hz (IQR: 0.23 – 0.32Hz) at 20Hz stimulation (Mann-Whitney p = 1.08e-53; Cliff's |δ| = 0.564, "large" effect size; Fig. 7D, right). The smaller effect size in knockout relative to control (Cliff's |δ| = 0.715), together with significant main effects of genotype (p = 1.38e-100), frequency (p = 6.68e-142), and a genotype × frequency interaction (p = 6.18e-06), confirmed impaired discrimination in the knockout model.

During 0-0.5s window, there was no significant change in PYRs' median firing rate in response to 2Hz vs. 20Hz stimulation of odor Mix in the knockout model (2Hz: 0.31Hz, IQR: 0.25 – 0.37Hz; 20Hz: 0.31Hz, IQR: 0.24 – 0.38Hz; Mann-Whitney p = 0.72; Cliff's |δ| = 0.0131, "negligible" effect

size; Fig. 7E, left). In contrast, firing rate in control varied significantly across stimulation frequencies (Mann-Whitney p = 2.7e-05; Cliff's |δ| = 0.153; two-way mixed RM ART-ANOVA: Control vs. Knockout, p = 1.27e-57; 2Hz vs. 20Hz stimulation, p = 0.00076; and interaction, p = 0.0043), demonstrating substantially weaker discrimination in the knockout model. During the 0-2s window, changes in PYRs firing rate in knockout model (2Hz: 0.39Hz, IQR: 0.35 – 0.43Hz; 20Hz: 0.36Hz, IQR: 0.31 – 0.40Hz; Mann-Whitney p = 3e-15; Cliff's |δ| = 0.288, "small" effect size; Fig. 7E, right) was similar to that observed in control (Control vs. Knockout, p = 3.18e-155; 2Hz vs. 20Hz stimulation, p = 8.19e-24; and interaction, p = 0.4946; two-way mixed RM ART-ANOVA).

Next, upon the removal of reciprocal connections between pyramidal neurons, the PYR-PYR knockout model exhibited enhanced discrimination relative to the control for odor A in the 0-2s time window. Conversely, discrimination was compromised in the case of odor B across both the time windows, while for odor Mix, it remained comparable to control.

For odor A, during the 0-0.5s window, the knockout model strongly discriminated between the odor frequencies (2Hz: 0.29Hz, IQR: 0.23 – 0.36Hz; 20Hz: 0.41Hz, IQR: 0.34 – 0.48Hz; Mann-Whitney p = 1.48e-62; Cliff's |δ| = 0.61, "large" effect size; Fig. 8C, left). A two-way mixed repeated-measures ART-ANOVA revealed main effects of genotype (p = 9.46e-59) and frequency (p = 2.1e-111) but not interaction (p = 0.2068), suggesting that discrimination was similar to the control. However, during the 0-2s window, the knockout model exhibited enhanced discrimination (2Hz: 0.37Hz, IQR: 0.33 – 0.42Hz; 20Hz: 0.45Hz, IQR: 0.40 – 0.49Hz; Mann-Whitney p = 1.57e-45; Cliff's |δ| = 0.517, "large" effect size; Fig. 8C, right) relative to control (Cliff's |δ| = 0.404) as evident by significant main and interaction effects by ART-ANOVA (genotype, p = 2.1e-129; frequency, p = 4.21e-72; interaction, p = 0.0074).

For odor B, during the 0-0.5s window, the knockout model showed impaired discrimination (2Hz: 0.36Hz, IQR: 0.29 – 0.42Hz; 20Hz: 0.27Hz, IQR: 0.22 – 0.34Hz; Mann-Whitney p = 2.94e-29; Cliff's |δ| = 0.41, "medium" effect size; Fig. 8D, left) relative to control (Cliff's |δ| = 0.512), as explained by significant main and interaction effects by ART-ANOVA (genotype, p = 7.63e-35; frequency, p = 1.98e-73; interaction, p = 0.0034). Similarly, during the 0-2s window, the knockout model again showed poor discrimination (2Hz: 0.37Hz, IQR: 0.32 – 0.41Hz; 20Hz: 0.29Hz, IQR: 0.24 – 0.33Hz;

Mann-Whitney p = 2.11e-69; Cliff's |δ| = 0.643, "large" effect size; Fig. 8D, right) relative to control (Cliff's |δ| = 0.715), as evident by significant main and interaction effects by ART-ANOVA (genotype, p = 3.36e-89; frequency, p = 8.92e-160; interaction, p = 0.0007).

For odor Mix, during the 0-0.5s window, the knockout model was unable to discriminate between two frequencies (2Hz: 0.30Hz, IQR: 0.23 – 0.37Hz; 20Hz: 0.31Hz, IQR: 0.25 – 0.39Hz; Mann-Whitney p = 0.00922; Cliff's |δ| = 0.0951, "negligible" effect size; Fig. 8E, left) similar to control (ART-ANOVA: genotype, p = 8.84e-58, frequency, p = 1.01e-06; and interaction, p = 0.1714).

During the 0-2s window, the knockout model exhibited similar discrimination (2Hz: 0.40Hz, IQR: 0.35 – 0.43Hz; 20Hz: 0.36Hz, IQR: 0.32 – 0.41Hz; Mann-Whitney p = 1.31e-11; Cliff's |δ| = 0.247, "small" effect size; Fig. 8E, right) as control (ART-ANOVA: genotype, p = 3.46e-146; frequency, p = 2.29e-20; interaction, p = 0.8723).

In summary, virtual knockout experiments demonstrated that eliminating direct inhibition onto PYRs enhanced frequency discrimination, whereas removing reciprocal connections between either pyramidal neurons or both types of interneurons simultaneously degraded decoding performance. Figure S7 and Table 4 provide a comprehensive summary of areas under the ROC curves (AUCs) for the CNNs and logistic regression classifiers, used to evaluate their performance across control and knockout model responses.

Circuit motifs, not just baseline activity level, determine odor frequency representation. Synaptic modifications resulted in changes to the baseline firing rates of PYRs. Knocking out the direct inhibition onto the PYRs increased the baseline firing from 1.09 ± 0.726Hz (Control) to 1.32 ± 0.792Hz (FF-PYR knockout) and 2.08 ± 0.991Hz (FB-PYR knockout) (Fig. 9B). In contrast, knocking out recurrent synaptic connections among PYRs (PYR-PYR knockout) and both kinds of interneurons (FF-FF and FB-FB knockout) decreased the baseline firing rate to 0.992 ± 0.692Hz and 0.963 ± 0.683Hz, respectively. Because change in frequency decoding accuracy correlated with baseline firing rate, we tested whether excitability alone could explain the decoding performance. To address this question, we modeled various control variants of the PCx network by systematically varying the spontaneous firing rates of pyramidal cells in the control network (Fig. 9A). The mean

spontaneous activity of the PYRs in these variant models spanned the entire range observed in the knockout models, with some variants exhibiting firing rates at the lower extreme and others at the upper extreme of the knockouts distribution (Fig. 9B). A complete comparative list of baseline firing rates for each network model is provided in Table 5. We then performed odor frequency decoding using PYR population responses from control variants (Fig. 9C) and compared them with those obtained from the knockout models (Fig. 9D) across all odor conditions. The CNN models' performance using the activity data from the knockout models showed a correlation between enhancement or impairment of odor frequency classification and their mean population baseline firing rates relative to the control network across all odor conditions (Fig. 9D). In contrast, control variants showed either minimal differences in classification performance for odors A and B, or an entirely reversed correlation for odor Mix (Fig. 9C). This suggests that specific circuit motifs, and not just baseline excitability, are important for the PCx network to discriminate odor frequency.

Overall, our analysis indicates that specific intracortical motifs, rather than merely changes in baseline excitability, are critical for shaping odor frequency representation.

Discussion

Mammalian and insect olfactory systems have long been recognized for their ability to encode chemical and physical properties of odor stimuli, such as odor identity, intensity, and concentration (60). These systems also exhibit a remarkable capacity to encode the temporal structure of olfactory cues present in natural odor landscapes to guide behavioral decisions in everyday ethological activities such as foraging, navigation, and locating odor sources (1,3–5,9,61). A recent study in mice showed that mitral/tufted (M/T) cells in the OB can encode odor frequencies up to 20Hz (19). However, whether cortical regions downstream of the OB, particularly the piriform cortex (PCx), participate in odor frequency encoding remains unclear. We investigated whether the PCx is capable of encoding odor stimulus frequencies. In our study, we used previously recorded *in vivo* activity from M/Ts in response to odor stimuli at 2Hz and 20Hz frequencies (19) as input to a biophysically relevant

PCx network model. We found that the PCx network model has the capacity to differentially encode the 2Hz and 20Hz odor stimulus frequencies.

We then simulated several synaptic knockout variants of the PCx model to assess how frequency encoding is affected by circuit perturbations, hence interrogating their significance. We found that removing either feedforward or feedback inhibition from pyramidal neurons enhanced the odor frequency classification accuracy compared to the control PCx model. In contrast, knocking out either recurrent excitation onto PYRs or recurrent inhibition onto both feedforward (FF) and feedback (FB) interneurons resulted in slightly impaired classification performance. Notably, decoding performance remained comparable to the control when either FF–FF or FB–FB intra-inhibitory connections were removed individually.

Overall, our results indicate the piriform cortex circuit is capable of encoding odor frequency using distinct circuit mechanisms.

Single-cell vs. population coding

We initially sought to understand how individual pyramidal cells represent odor-frequency. To study this, we used a cellular-level statistical approach based on the average spiking rates of the individual pyramidal neurons across 336 trials to classify them into frequency-discriminating and non-discriminating types (Mann-Whitney U test; Bonferroni correction). We found that pyramidal neurons at the individual level are inadequate to encode odor stimulation frequencies. Moreover, this type of encoding would result in a low-dimensional representation of a given parameter such as odor-frequency, in a systematically patterned network (62). However, prior studies indicate that multiple neurons often respond nonlinearly to represent a given stimulus parameter, which in turn helps the organism to perceive it (63–65). Overall, this approach is only partially predictive of a cell's importance for representing a given feature (66).

Therefore, we turned our attention to the population-level decoding of frequency information. Initially, the collective activity of all the PYRs, based on the mean firing rate over 336 trials, was quite effective in discriminating between the two stimulation frequencies (Fig. 1F-H). However, as

part of a network, activities of the individual neurons are correlated with each other over time. Stefanini et al. (2020) experimentally demonstrated that due to this correlation, a decoder might assign larger weights to the weakly tuned or even untuned neurons when their activities are correlated with tuned neurons. Population decoders (pattern classifiers) using the average firing rate of neurons have been extensively used in different fields of neuroscience to predict decision boundaries from experimental outcomes. However, averaging spiking activity over long periods results in the loss of valuable information embedded in the temporal structure of the firing patterns of the neuronal population. To preserve this rich information, we employed one-dimensional convolutional neural network models (1-D CNNs), and logistic regression classifiers for odor frequency classification. These models take the binned spiking activities of neurons across the entire stimulation period as input, using 20ms non-overlapping time windows. Each bin represents a specific 20ms time interval and is assigned a binary value (0 or 1) to indicate whether a neuron spiked within that interval. The 20ms bin size was selected to maximize the likelihood of capturing no more than one spike per bin. Both non-linear and linear models trained and tested on PYRs' activity, reliably distinguished odor stimulus frequency (Fig. 2B,D; S6; S7).

Using the trial-averaged (n=300) log-likelihood difference (ΔLL) for each neuron, we ranked neurons according to their importance/contribution to frequency decoding (Fig. 2C). We observed that the contribution of individual PYRs was largely similar across the population. This corroborates with our earlier observation from the single-cell analysis that odor-frequency discrimination does not predominantly occur at the level of individual neurons in the PCx.

Overall, these analyses indicate that odor frequency encoding is a robust capability of the PCx network and is highly distributed across the PYR population.

The encoding role of circuit motifs

Cellular and circuit elements, essentially interneurons, have been observed to play key roles in modifying network outputs in other brain areas, such as the hippocampus (67,68). Different circuit motifs differentially shape PCx responses (57). Several experiments have elucidated the role of

inhibitory and recurrent circuitry in encoding the temporally dynamic structure of odor stimuli in the olfactory circuit (19,23,69–72). These effects can emerge through both spiking patterns and subthreshold membrane potential dynamics. Active neurons are generally observed to contribute to stimulus encoding, as stimulus-evoked deviations from baseline activity are critical for encoding. Previous work has shown that the importance of a cell within an encoding population is strongly correlated with its average response property (66). A neuron's average response is shaped by the balance of excitatory and inhibitory inputs it receives. We tested this by altering the baseline noise current to modulate the baseline firing of the PYR population to match the levels observed in different knockout cases (Fig. 9). However, such a general modulation in baseline activity could not achieve decoding accuracy similar to that of the knockout models. This indicated that specific circuit motifs that are intertwined with the pyramidal cells of the piriform cortex both spatially and temporally, sculpt the network response and are therefore necessary for specific modulation of decoding performance. Experimental and theoretical studies will be required in the future to understand how each of these circuit motifs is able to modulate decoding performance of the PCx network.

Thus, our findings from various knockout models suggest that the odor-frequency representation in the piriform cortex depends on specific circuit motifs.

Limitations of our model circuit

The current model simplifies PCx circuitry by not differentiating among various neuronal subtypes. We did not distinguish between different subclasses of principal neurons (e.g. semilunar cells vs. superficial pyramidal cells), feedforward interneurons (e.g., horizontal cells vs. neurogliaform cells) and feedback interneurons (e.g. regular-spiking multipolar vs. fast-spiking multipolar vs. bitufted vs. neurogliaform cells). Semilunar and superficial pyramidal neurons are functionally distinct subtypes due to their specialization in afferent and intracortical processing, respectively (45). Additionally, distinct interneuron subtypes contribute to layer-specific phasic inhibition of layer II principal neurons and hence play specific roles in cortical odor processing (43). In our model circuit we did not incorporate the centrifugal/feedback projections from the PCx back to the OB. These cortical feedback projections provide strongly normalized activity over diverse

olfactory stimuli, which can be combined with the highly unbalanced activities of OSNs to influence M/T responses (30). The range of odor stimuli in our simulations was also limited in terms of mixture complexity, concentration, and frequency range. It would be intriguing to investigate the impact of these parameters on the frequency encoding capacity of the PCx. For instance, throughout our results, we observed poor decoding of odor frequency responses for odor Mix compared to odor A and B.

Overall, our results suggest that the PCx network has the capacity to encode odor frequencies associated with naturalistic odor stimuli. Experimental validation of these findings would be valuable, as temporal dynamics in sensory stimuli are thought to be an important route of information transfer to the brain.

Supplemental material

Supplemental Figures S1-S7: https://github.com/ankitbishnoe29/Supplemental-Figures

Acknowledgments

Preprint is available at https://doi.org/10.1101/2025.07.14.664633. This research utilized the High-Performance Cluster (Param Sanganak) facilities at the Computer Centre, IIT Kanpur.

Grants

The work was supported by a Ramalingaswami fellowship from the Department of Biotechnology, India (BT/RLF/Re-entry/14/2022); a grant from Ignite Life Science Foundation (IGNITE/NDGN/2025/001); a PMECRG grant from Anusandhan National Research Foundation, India (ANRF/ECRG/2024/006274/LS) and a startup grant from the Indian Institute of Technology (IIT) Kanpur awarded to Debanjan Dasgupta. Ankit Kumar received a fellowship for his M.Tech from the Ministry of Education, India.

Disclosures

The authors declare no competing financial interests.

Disclaimers

The content is solely the responsibility of the authors and does not necessarily represent the official views of Indian Institute of Technology, Kanpur, 208016, India.

Author Contributions

A.K. conceived and designed research, performed experiments, analyzed data, interpreted results of experiments, prepared figures, drafted manuscript, edited and revised manuscript, and approved final version of manuscript; O.C. performed experiments, and analyzed data; M.J. performed experiments, and analyzed data; A.M. conceived and designed research; D.D. conceived and designed research, interpreted results of experiments, drafted manuscript, edited and revised manuscript, and approved final version of manuscript.

References

1. Murlis J, Elkinton J, entomology RCA review of, 1992 undefined. Odor plumes and how insects use them. researchgate.netJ Murlis, JS Elkinton, RT CardeAnnual review of entomology, 1992•researchgate.net [Internet]. 2003 [cited 2025 Jan 30];37:505–37. Available from: https://www.researchgate.net/profile/Ring-Carde/publication/234150143_Odor_Plumes_and_How_Insects_Use_Them/links/00b7d52bcdfc033642000000/Odor-Plumes-and-How-Insects-Use-Them.pdf

2. Koehl MAR. The Fluid Mechanics of Arthropod Sniffing in Turbulent Odor Plumes. Chem Senses [Internet]. 2006 Feb 1 [cited 2025 Feb 24];31(2):93–105. Available from: https://dx.doi.org/10.1093/chemse/bjj009

3. Ackels T, Erskine A, Dasgupta D, Marin AC, Warner TPA, Tootoonian S, et al. Fast odour dynamics are encoded in the olfactory system and guide behaviour. Nature 2021 593:7860 [Internet]. 2021 May 5 [cited 2025 Jan 23];593(7860):558–63. Available from: https://www.nature.com/articles/s41586-021-03514-2

4. Celani A, Villermaux E, Vergassola M. Odor landscapes in turbulent environments. Phys Rev X [Internet]. 2014 Oct 28 [cited 2025 Feb 24];4(4):041015. Available from: https://journals.aps.org/prx/abstract/10.1103/PhysRevX.4.041015

5. Mylne KR, Mason PJ. Concentration fluctuation measurements in a dispersing plume at a range of up to 1000 m. Quarterly Journal of the Royal Meteorological Society [Internet]. 1991 Jan 1 [cited 2025 Jan 30];117(497):177–206. Available from: https://onlinelibrary.wiley.com/doi/full/10.1002/qj.49711749709

6. Shralman BI, Siggia ED. Scalar turbulence. Nature 2000 405:6787 [Internet]. 2000 Jun 8 [cited 2025 Feb 24];405(6787):639–46. Available from: https://www.nature.com/articles/35015000

7. Marin AC, Schaefer AT, Ackels T. Spatial information from the odour environment in mammalian olfaction. Cell Tissue Res [Internet]. 2021 Jan 1 [cited 2025 May 10];383(1):473. Available from: https://pmc.ncbi.nlm.nih.gov/articles/PMC7872987/

8. Crimaldi J, Lei H, Schaefer A, Schmuker M, Smith BH, True AC, et al. Active sensing in a dynamic olfactory world. J Comput Neurosci [Internet]. 2022 Feb 1 [cited 2025 Feb 24];50(1):1–6. Available from: https://link.springer.com/article/10.1007/s10827-021-00798-1

9. Marin AC, Schaefer AT, Ackels T. Spatial information from the odour environment in mammalian olfaction. Cell Tissue Res [Internet]. 2021 Jan 1 [cited 2025 Feb 24];383(1):473–83. Available from: https://pubmed.ncbi.nlm.nih.gov/33515294/

10. Szyszka P. Odor coding and neural plasticity in the mushroom body of the honeybee. 2005 Feb 22 [cited 2025 May 10]; Available from: https://refubium.fu-berlin.de/handle/fub188/12883

11. Gumaste A, Baker KL, Izydorczak M, True AC, Vasan G, Crimaldi JP, et al. Behavioral discrimination and olfactory bulb encoding of odor plume intermittency. Elife. 2024 Mar 5;12.

12. Wu Y, Chen K, Xing C, Huang M, Zhao K, Zhou W. Human olfactory perception embeds fine temporal resolution within a single sniff. Nature Human Behaviour 2024 8:11 [Internet]. 2024 Oct 14 [cited 2025 Jul 1];8(11):2168–78. Available from: https://www.nature.com/articles/s41562-024-01984-8

13. Vickers NJ. Mechanisms of animal navigation in odor plumes. https://doi.org/102307/1542524 [Internet]. 2000 Apr 1 [cited 2025 Jan 30];198(2):203–12. Available from: https://www.journals.uchicago.edu/doi/10.2307/1542524

14. Laurent G, Wehr M, Davidowitz H. Temporal Representations of Odors in an Olfactory Network. The Journal of Neuroscience [Internet]. 1996 [cited 2025 May 10];16(12):3837. Available from: https://pmc.ncbi.nlm.nih.gov/articles/PMC6578619/

15. Vickers NJ, Baker TC. Reiterative responses to single strands of odor promote sustained upwind flight and odor source location by moths. Proceedings of the National Academy of Sciences [Internet]. 1994 Jun 21 [cited 2025 Feb 24];91(13):5756–60. Available from: https://www.pnas.org/doi/abs/10.1073/pnas.91.13.5756

16. Vickers NJ, Christensen TA, Baker TC, Hildebrand JG. Odour-plume dynamics influence the brain's olfactory code. Nature [Internet]. 2001 Mar 22 [cited 2025 Feb 24];410(6827):466–70. Available from: https://pubmed.ncbi.nlm.nih.gov/11260713/

17. Huston SJ, Stopfer M, Cassenaer S, Aldworth ZN, Laurent G. Neural Encoding of Odors during Active Sampling and in Turbulent Plumes. Neuron. 2015 Oct 21;88(2):403–18.

18. Lucas P, Lei H, Olsson SB, Pannunzi M, Nowotny T. Odor Stimuli: Not Just Chemical Identity. Front Physiol [Internet]. 2019 Nov 27 [cited 2025 Feb 24];10:1428. Available from: https://pmc.ncbi.nlm.nih.gov/articles/PMC6890726/

19. Dasgupta D, Warner TPA, Erskine A, Schaefer AT. Coupling of Mouse Olfactory Bulb Projection Neurons to Fluctuating Odor Pulses. Journal of Neuroscience [Internet]. 2022 May 25 [cited 2025 Jan 23];42(21):4278–96. Available from: https://www.jneurosci.org/content/42/21/4278

20. Lewis SM, Suarez LM, Rigolli N, Franks KM, Steinmetz NA, Gire DH. The spiking output of the mouse olfactory bulb encodes large-scale temporal features of natural odor environments. bioRxiv [Internet]. 2024 Mar 5 [cited 2025 Jul 8];2024.03.01.582978. Available from: https://www.biorxiv.org/content/10.1101/2024.03.01.582978v1

21. Duchamp-Viret P, Chaput MA, Duchamp A. Odor Response Properties of Rat Olfactory Receptor Neurons. Science (1979) [Internet]. 1999 Jun 25 [cited 2025 Jul 1];284(5423):2171–9. Available from: https://www.science.org/doi/10.1126/science.284.5423.2171

22. Bolding KA, Franks KM. Complementary codes for odor identity and intensity in olfactory cortex. Elife. 2017 Apr 5;6.

23. Bolding KA, Nagappan S, Han BX, Wang F, Franks KM. Recurrent circuitry is required to stabilize piriform cortex odor representations across brain states. Elife. 2020 Jul 1;9:1–23.

24. Franks KM, Russo MJ, Sosulski DL, Mulligan AA, Siegelbaum SA, Axel R. Recurrent circuitry dynamically shapes the activation of piriform cortex. Neuron [Internet]. 2011 Oct 6 [cited 2025 Jun 8];72(1):49. Available from: https://pmc.ncbi.nlm.nih.gov/articles/PMC3219421/

25. Haberly LB. Parallel-distributed Processing in Olfactory Cortex: New Insights from Morphological and Physiological Analysis of Neuronal Circuitry. Chem Senses [Internet]. 2001 Jun 1 [cited 2025 Dec 10];26(5):551–76. Available from: https://dx.doi.org/10.1093/chemse/26.5.551

26. Haberly LB, Bower JM. Olfactory cortex: model circuit for study of associative memory? Trends Neurosci [Internet]. 1989 Jan 1 [cited 2025 Dec 10];12(7):258–64. Available from: https://www.cell.com/action/showFullText?pii=0166223689900258

27. Linster C, Hasselmo ME. Neuromodulation and the Functional Dynamics of Piriform Cortex. Chem Senses [Internet]. 2001 Jun 1 [cited 2025 Dec 10];26(5):585–94. Available from: https://dx.doi.org/10.1093/chemse/26.5.585

28. Saar D, Grossman Y, Barkai E. Learning-Induced Enhancement of Postsynaptic Potentials in Pyramidal Neurons. https://doi.org/101152/jn20028752358 [Internet]. 2002 [cited 2025 Dec 10];87(5):2358–63. Available from: /doi/pdf/10.1152/jn.2002.87.5.2358?download=true

29. Wilson DA, Stevenson RJ. The fundamental role of memory in olfactory perception. Trends Neurosci [Internet]. 2003 May 1 [cited 2025 Dec 10];26(5):243–7. Available from: https://www.cell.com/action/showFullText?pii=S0166223603000766

30. Zak JD, Reddy G, Konanur V, Murthy VN. Distinct information conveyed to the olfactory bulb by feedforward input from the nose and feedback from the cortex. Nature Communications 2024 15:1 [Internet]. 2024 Apr 16 [cited 2025 Feb 13];15(1):1–16. Available from: https://www.nature.com/articles/s41467-024-47366-6

31. Mori K, Sakano H. Olfactory Circuitry and Behavioral Decisions. Annu Rev Physiol [Internet]. 2021 Feb 10 [cited 2025 Jul 8];83(Volume 83, 2021):231–56. Available from: https://www.annualreviews.org/content/journals/10.1146/annurev-physiol-031820-092824

32. Fischler-Ruiz W, Clark DG, Joshi NR, Devi-Chou V, Kitch L, Schnitzer M, et al. Olfactory landmarks and path integration converge to form a cognitive spatial map. Neuron [Internet]. 2021 Dec 15 [cited 2025 Jul 8];109(24):4036-4049.e5. Available from: https://pubmed.ncbi.nlm.nih.gov/34710366/

33. Carnevale T, Hines M. The NEURON Book. 2005 [cited 2025 Jul 8]; Available from: www.cambridge.org

34. Linster C, Menon A V., Singh CY, Wilson DA. Odor-specific habituation arises from interaction of afferent synaptic adaptation and intrinsic synaptic potentiation in olfactory cortex. Learning & Memory [Internet]. 2009 Jul 1 [cited 2025 Jan 21];16(7):452–9. Available from: http://learnmem.cshlp.org/content/16/7/452.full

35. Isaacson JS. Odor representations in mammalian cortical circuits. Curr Opin Neurobiol. 2010 Jun 1;20(3):328–31.

36. Poo C, Isaacson JS. Odor Representations in Olfactory Cortex: “Sparse” Coding, Global Inhibition, and Oscillations. Neuron [Internet]. 2009 Jun 25 [cited 2025 Feb 13];62(6):850–61. Available from: http://www.cell.com/article/S0896627309003973/fulltext

37. Stokes CCA, Isaacson JS. From Dendrite to Soma: Dynamic Routing of Inhibition by Complementary Interneuron Microcircuits in Olfactory Cortex. Neuron [Internet]. 2010 Aug 12 [cited 2025 Jan 21];67(3):452–65. Available from: http://www.cell.com/article/S0896627310005131/fulltext

38. Stokes CCA, Isaacson JS. From Dendrite to Soma: Dynamic Routing of Inhibition by Complementary Interneuron Microcircuits in Olfactory Cortex. Neuron. 2010 Aug 12;67(3):452–65.

39. Migliore M, Hoffman DA, Magee JC, Johnston D. Role of an A-type K+ conductance in the back-propagation of action potentials in the dendrites of hippocampal pyramidal neurons. J Comput Neurosci [Internet]. 1999 [cited 2025 Jan 27];7(1):5–15. Available from: https://modeldb.science/2796

40. Bathellier B, Margrie TW, Larkum ME. Properties of Piriform Cortex Pyramidal Cell Dendrites: Implications for Olfactory Circuit Design. Journal of Neuroscience [Internet]. 2009 Oct 7 [cited 2025 Jan 28];29(40):12641–52. Available from: https://www.jneurosci.org/content/29/40/12641

41. Ikeda K, Suzuki N, Bekkers JM. Sodium and potassium conductances in principal neurons of the mouse piriform cortex: a quantitative description. J Physiol [Internet]. 2018 Nov 1 [cited 2025 Jan 28];596(22):5397–414. Available from: https://onlinelibrary.wiley.com/doi/full/10.1113/JP275824

42. Wang XJ, Buzsáki G. Gamma Oscillation by Synaptic Inhibition in a Hippocampal Interneuronal Network Model. Journal of Neuroscience [Internet]. 1996 Oct 15 [cited 2025 Jan 27];16(20):6402–13. Available from: https://www.jneurosci.org/content/16/20/6402

43. Suzuki N, Bekkers JM. Distinctive Classes of GABAergic Interneurons Provide Layer-Specific Phasic Inhibition in the Anterior Piriform Cortex. 2010;

44. Suzuki N, cortex JBC, 2010 undefined. Distinctive classes of GABAergic interneurons provide layer-specific phasic inhibition in the anterior piriform cortex. academic.oup.comN Suzuki, JM BekkersCerebral cortex, 2010•academic.oup.com [Internet]. 2010 [cited 2025 Jan 28]; Available from: https://academic.oup.com/cercor/article-abstract/20/12/2971/367693

45. Suzuki N, Bekkers JM. Two Layers of Synaptic Processing by Principal Neurons in Piriform Cortex. Journal of Neuroscience [Internet]. 2011 Feb 9 [cited 2025 Jun 4];31(6):2156–66. Available from: https://www.jneurosci.org/content/31/6/2156

46. Stern M, Bolding KA, Abbott LF, Franks KM. A transformation from temporal to ensemble coding in a model of piriform cortex. Elife. 2018 Mar 29;7.

47. Meissel K, Yao ES. Using Cliff’s Delta as a Non-Parametric Effect Size Measure: An Accessible Web App and R Tutorial. 2024 [cited 2025 Oct 9];29. Available from: https://cliffdelta.shinyapps.io/calculator;

48. ORDINAL METHODS FOR BEHAVIORAL DATA ANALYSIS.

49. Appropriate Statistics for Ordinal Level Data: Should We Really Be Using t-test and Cohen’s d for Evaluating Group Differences on the NSSE and other Surveys? [Internet]. [cited 2025 Oct 9]. Available from:

https://www.researchgate.net/publication/237544991_Appropriate_Statistics_for_Ordinal_Level_Data_Should_We_Really_Be_Using_t-test_and_Cohen's_d_for_Evaluating_Group_Differences_on_the_NSSE_and_other_Surveys

50. Salter KC, Fawcett RF. The ART test of interaction: a robust and powerful rank test of interaction in factorial models. Commun Stat Simul Comput. 1993 Jan 1;22(1):137–53.

51. Higgins JJ, Blair RC, Tashtoush S. THE ALIGNED RANK TRANSFORM PROCEDURE. Conference on Applied Statistics in Agriculture [Internet]. 1990 Apr 26 [cited 2025 Oct 10]; Available from: https://newprairiepress.org/agstatconference/1990/proceedings/18

52. A Class of Rank Order Tests for a General Linear Hypothesis on JSTOR [Internet]. [cited 2025 Oct 10]. Available from: https://www.jstor.org/stable/2239597

53. Jr. JLH, Lehmann EL. Rank Methods for Combination of Independent Experiments in Analysis of Variance. https://doi.org/101214/aoms/1177704575 [Internet]. 1962 Jun 1 [cited 2025 Oct 10];33(2):482–97. Available from: https://projecteuclid.org/journals/annals-of-mathematical-statistics/volume-33/issue-2/Rank-Methods-for-Combination-of-Independent-Experiments-in-Analysis-of/10.1214/aoms/1177704575.full

54. Conover WJ, Iman RL. Rank Transformations as a Bridge Between Parametric and Nonparametric Statistics. Am Stat. 1981 Aug;35(3):124.

55. Bekkers JM, Suzuki N. Neurons and circuits for odor processing in the piriform cortex. Trends Neurosci [Internet]. 2013 Jul 1 [cited 2025 Jan 31];36(7):429–38. Available from: http://www.cell.com/article/S0166223613000660/fulltext

56. de Almeida L, Idiart M, Linster C. A model of cholinergic modulation in olfactory bulb and piriform cortex. J Neurophysiol [Internet]. 2013 [cited 2025 Jan 23];109(5):1360–77. Available from: https://journals.physiology.org/doi/10.1152/jn.00577.2012

57. Stern M, Bolding KA, Abbott LF, Franks KM. A transformation from temporal to ensemble coding in a model of piriform cortex. Elife. 2018 Mar 29;7.

58. Bolding KA, Franks KM. Recurrent cortical circuits implement concentration-invariant odor coding. [cited 2025 Nov 24]; Available from: www.sciencemag.org/content/361/6407/eaat6904/suppl/DC1

59. Cliff N. Dominance statistics: Ordinal analyses to answer ordinal questions. Psychol Bull. 1993;114(3):494–509.

60. Su CY, Menuz K, Carlson JR. Olfactory Perception: Receptors, Cells, and Circuits. Cell [Internet]. 2009 Oct 2 [cited 2025 May 18];139(1):45–59. Available from: https://www.cell.com/action/showFullText?pii=S0092867409011751

61. Hopfield JJ. Olfactory computation and object perception. Proceedings of the National Academy of Sciences [Internet]. 1991 Aug 1 [cited 2025 Jan 30];88(15):6462–6. Available from: https://www.pnas.org/doi/abs/10.1073/pnas.88.15.6462

62. Fusi S, Miller EK, Rigotti M. Why neurons mix: high dimensionality for higher cognition. Curr Opin Neurobiol [Internet]. 2016 Apr 1 [cited 2025 May 20];37:66–74. Available from: https://www.sciencedirect.com/science/article/pii/S0959438816000118

63. Saxena S, Cunningham JP. Towards the neural population doctrine. Curr Opin Neurobiol [Internet]. 2019 Apr 1 [cited 2025 May 20];55:103–11. Available from: https://www.sciencedirect.com/science/article/pii/S0959438818300990

64. Kriegeskorte N, Douglas PK. Interpreting encoding and decoding models. Curr Opin Neurobiol [Internet]. 2019 Apr 1 [cited 2025 May 20];55:167–79. Available from: https://www.sciencedirect.com/science/article/pii/S0959438818301004

65. Rigotti M, Barak O, Warden MR, Wang XJ, Daw ND, Miller EK, et al. The importance of mixed selectivity in complex cognitive tasks. Nature [Internet]. 2013 May 30 [cited 2025 May 20];497(7451):585–90. Available from: https://www.nature.com/articles/nature12160

66. Stefanini F, Kushnir L, Jimenez JC, Jennings JH, Woods NI, Stuber GD, et al. A Distributed Neural Code in the Dentate Gyrus and in CA1. Neuron [Internet]. 2020 Aug 19 [cited 2025 May 19];107(4):703-716.e4. Available from: https://www.sciencedirect.com/science/article/pii/S0896627320303913

67. Dasgupta D, Sikdar SK. Calcium permeable AMPA receptor-dependent long lasting plasticity of intrinsic excitability in fast spiking interneurons of the dentate gyrus decreases inhibition in the granule cell layer. Hippocampus [Internet]. 2015 Mar 1 [cited 2025 Jul 11];25(3):269–85. Available from: https://onlinelibrary.wiley.com/doi/full/10.1002/hipo.22371

68. Dasgupta D, Sikdar SK. Heterogeneous network dynamics in an excitatory-inhibitory network model by distinct intrinsic mechanisms in the fast spiking interneurons. Brain Res [Internet]. 2019 Jul 1 [cited 2025 Jul 11];1714:27–44. Available from: https://pubmed.ncbi.nlm.nih.gov/30771318/

69. Nagel KI, Hong EJ, Wilson RI. Synaptic and circuit mechanisms promoting broadband transmission of olfactory stimulus dynamics. Nat Neurosci [Internet]. 2015 Jan 1 [cited 2025 May 18];18(1):56–65. Available from: https://pubmed.ncbi.nlm.nih.gov/25485755/

70. Burton SD. Inhibitory circuits of the mammalian main olfactory bulb. J Neurophysiol [Internet]. 2017 Oct 1 [cited 2025 Feb 13];118(4):2034–51. Available from: https://journals.physiology.org/doi/10.1152/jn.00109.2017

71. Abraham NM, Egger V, Shimshek DR, Renden R, Fukunaga I, Sprengel R, et al. Synaptic Inhibition in the Olfactory Bulb Accelerates Odor Discrimination in Mice. Neuron [Internet]. 2010 Feb 11 [cited 2025 Dec 11];65(3):399–411. Available from: https://pubmed.ncbi.nlm.nih.gov/20159452/

72. Kolling LJ, Tatti R, Lowry T, Loeven AM, Fadool JM, Fadool DA. Modulating the Excitability of Olfactory Output Neurons Affects Whole-Body Metabolism. J Neurosci [Internet]. 2022 Jul 27 [cited 2025 Dec 11];42(30):5966–90. Available from: https://pubmed.ncbi.nlm.nih.gov/35710623/

Figure Legends

Figure 1. PCx neurons discriminate between odor identities and frequencies at network level. **A,** Schematic of the piriform cortex (PCx) network model. **B,** Representative voltage traces from three model pyramidal neurons (PYRs) in response to the three odor mixtures (A, B, and Mix) presented at 2Hz (blue) and 20Hz (red) frequencies. **C,** Violin plots showing the distribution of mean firing rates (averaged across 336 trials per neuron) after baseline subtraction during the initial 500ms of odor stimulation at 2Hz and 20Hz: Mix vs. A; (**D**)**,** Mix vs. B; and (**E**)**;** A vs. B; statistical significance was tested using two-tailed Mann-Whitney U test, and effect sizes were calculated using Cliff's delta (δ) (n = 500 neurons). In each violin plot, the central solid marker represents the median while the whiskers represent the first and third quartiles. **F,** Violin plots showing the distribution of mean firing rates (averaged across 336 trials per neuron) after baseline subtraction in response to odor A at 2Hz vs. 20Hz, **(G),** odor B 2Hz vs. 20Hz, and **(H),** odor Mix 2Hz vs. 20Hz. The time bins represent the odor stimulation period used for the analysis (0-500ms and 0-2s). Statistical tests were performed in a similar way as described in Fig.1 C-E. **I,** Stacked bar plots depicting effect size magnitudes among pyramidal neurons with significant firing rate differences between 2Hz and 20Hz stimulation ($p < 0.05$, two-tailed Mann-Whitney U test comparing 336 trials per frequency per neuron) for odor A, **(J),** odor B, and **(K),** odor Mix during the 0–0.5s and 0–2s post-stimulus windows. Each bar represents discriminating neurons stratified by Cliff's delta (δ) magnitude: negligible ($|\delta| < 0.147$; grey), small ($0.147 \leq |\delta| < 0.33$; black), medium ($0.33 \leq |\delta| < 0.474$; purple), and large ($|\delta| \geq 0.474$; green). Note that none of the conditions showed any cells with medium or large magnitude differences.

Figure 2. One-dimensional convolutional neural network models (1-D CNNs) and logistic regression classifiers demonstrate that PCx network activity can discriminate odor-frequency. **A,** Schematic showing the preparation of datasets using spike times of PYRs during the entire 2s odor stimulation period and the configuration of 1-D CNN for odor-frequency classification. **B,** Average classification accuracy of CNN models in discriminating 2Hz vs. 20Hz stimulation for odor A (left), odor B (center), and odor Mix (right) as a function of pyramidal neuron (PYR) population size (population

step size = 50). The solid line and shaded area represent the mean and the corresponding standard deviation, respectively, from 144 iterations of randomly sampled neurons. Chance-level accuracy was estimated by randomly shuffling trial labels (grey lines). **C,** Plots showing the difference in log-likelihood values (ΔLL) of CNN model between intact and perturbed test sets for each neuron in the descending order of their importance for frequency decoding (2Hz vs. 20Hz) for odor A (top), odor B (middle), and odor Mix (bottom). In the perturbed test set, a neuron's spiking activity was replaced by its baseline activity. The solid lines and the shaded region have similar meaning as in Fig. 2B (n = 300 iterations). **D,** Average classification accuracy of logistic regression classifiers in discriminating 2Hz vs. 20Hz stimulation for odor A (magenta), odor B (green), and odor Mix (orange) as a function of PYR population size (population step size = 25). For each population size, neurons were randomly sampled in 144 independent iterations. Solid lines represent the mean, and the shaded region represents the corresponding standard deviation. Chance-level accuracy was estimated by randomly shuffling trial labels (grey lines).

Figure 3. Eliminating the feedforward inhibition (FF) onto PYRs increases the frequency discrimination accuracy of the PCx network. **A,** Schematic of a PCx knockout model in which synaptic connections from feedforward interneurons (FFINs) onto pyramidal neurons (PYRs) were removed. Knocked-out synaptic connections are indicated by hollow triangles. **B,** Average frequency classification accuracy as a function of PYR population size, using outputs from the control (blue) and knockout (red) network models. Solid lines represent the mean, and the shaded regions represent the corresponding standard deviation (n = 144). Grey lines represent mean accuracy obtained from the shuffled controls with their corresponding SD. **C,** Violin plots of baseline-corrected mean firing rates (averaged across 336 trials per neuron, n = 500) comparing knockout vs. control PCx models in response to 2Hz and 20Hz stimulation with odor A; (**D**) odor B; and (**E**) odor Mix, during 0-0.5s (left), and 0-2s (right) of the stimulus windows. Statistical significance of the 2Hz vs. 20Hz comparison was tested using two-tailed Mann-Whitney U tests, and effect sizes were calculated using Cliff's delta (δ) (*n* = 500 neurons). Two-way mixed repeated measures ART ANOVA with genotype and frequency as factors.

Figure 4. Eliminating feedback inhibition onto PYRs increases the frequency discrimination accuracy of the PCx network model. **A,** Schematic of the PCx knockout model in which synaptic connections from feedback interneurons (FBINs) onto pyramidal neurons (PYRs) were removed. The knocked-out synaptic connections are indicated by hollow triangles. **B,** Odor frequency classification accuracy as a function of PYRs population size in control (blue) and knockout (red) PCx using 1-D convolutional neural network models. Data are shown as mean ± SD from 144 iterations. Grey lines represent mean accuracy obtained from the shuffled controls with their corresponding SD. **C,** Violin plots of baseline-corrected mean firing rates (averaged across 336 trials per neuron, n = 500) comparing knockout vs. control PCx models in response to 2Hz and 20Hz stimulation with odor A; (**D**) odor B; and (**E**) odor Mix, during 0-0.5s (left), and 0-2s (right) of the stimulus windows. Statistical tests were performed as described in Fig. 3C-E.

Figure 5. Eliminating recurrency among the FFINs mildly decreased frequency discrimination accuracy of the PCx network model. **A,** Schematic of PCx knockout model in which synaptic connections among feedforward interneurons (FFINs) were removed. Knocked-out synaptic connections are indicated by hollow triangles. **B,** Odor frequency discrimination accuracy as a function of PYRs population size in control (blue) and knockout (red) PCx using 1-D convolutional neural network models. Data are shown as mean ± SD from 144 iterations. Grey lines represent mean accuracy obtained from the shuffled controls with their corresponding SD. **C,** Violin plots of baseline-corrected mean firing rates (averaged across 336 trials per neuron, n = 500) comparing knockout vs. control PCx models in response to 2Hz and 20Hz stimulation of odor A; (**D**) odor B; and (**E**) odor Mix, during 0-0.5s (left), and 0-2s (right) post-stimulus windows. Statistical tests were performed as described in Fig. 3C-E.

Figure 6. Eliminating recurrency among the FBINs did not alter frequency discrimination accuracy of the PCx network model. **A,** Schematic of the PCx knockout model in which synaptic connections among feedback interneurons (FBINs) were removed. Knocked-out synaptic connections are indicated by hollow triangles. **B,** Odor frequency classification accuracy as a function of PYRs population size in control (blue) and knockout (red) PCx using 1-D convolutional neural network

models. Data are shown as mean ± SD from 144 iterations. Grey lines represent mean accuracy obtained from the shuffled controls with their corresponding SD. **C,** Violin plots of baseline-corrected mean firing rates (averaged across 336 trials per neuron, n = 500) comparing knockout vs. control PCx models in response to 2Hz and 20Hz stimulation of odor A; (**D**) odor B; and (**E**) odor Mix, during 0-0.5s (left), and 0-2s (right) post-stimulus windows. Statistical tests were performed as described in Fig. 3C-E.

Figure 7. Impairment of frequency discrimination accuracy of the PCx network model due to the elimination of recurrent inhibition within both FFINs and FBINs. **A,** Schematic of the PCx knockout model in which synaptic connections among both feedforward interneurons (FFINs) and feedback interneurons (FBINs) were removed. Knocked-out synaptic connections are indicated by hollow triangles. **B,** Odor frequency classification accuracy as a function of PYRs population size in control (blue) and knockout (red) PCx using 1-D convolutional neural network models. Data are shown as mean ± SD from 144 iterations. Grey lines represent mean accuracy obtained from the shuffled controls with their corresponding SD. **C,** Violin plots of baseline-corrected mean firing rates (averaged across 336 trials per neuron, n = 500) comparing knockout vs. control PCx models in response to 2Hz and 20Hz stimulation of odor A; (**D**) odor B; and (**E**) odor Mix, during 0-0.5s (left), and 0-2s (right) post-stimulus windows. Statistical tests were performed as described in Fig. 3C-E.

Figure 8. Eliminating recurrency among the PYRs decreased the frequency discrimination accuracy of the PCx network model. **A,** Schematic of the PCx knockout model in which recurrent synaptic connections among pyramidal neurons (PYRs) were removed. Knocked-out synaptic connections are indicated by hollow triangles. **B,** Odor frequency classification accuracy as a function of PYRs population size in control (blue) and knockout (red) PCx using 1-D convolutional neural network models. Data are shown as mean ± SD from 144 iterations. Grey lines represent mean accuracy obtained from the shuffled controls with their corresponding SD. **C,** Violin plots of baseline-corrected mean firing rates (averaged across 336 trials per neuron, n = 500) comparing knockout vs. control PCx models in response to 2Hz and 20Hz stimulation of odor A; (**D**) odor B; and (**E**) odor Mix,

during 0-0.5s (left), and 0-2s (right) post-stimulus windows. Statistical tests were performed as described in Fig. 3C-E.

Figure 9. Baseline firing rate does not determine odor frequency discrimination in the PCx. **A,** Example voltage traces from PYRs in control and variant networks (Control '-3' to Control '+3'), showing baseline activity levels modulated by varying the baseline noise, resulting in firing rates ranging from 0.635 ± 0.56 Hz to 2.98 ± 1.14 Hz (left to right). **B,** Baseline firing rates of the PYR population across control variants (left panel) and knockout models (right panel). Bar heights represent mean firing rates, and error bars indicate standard deviations (n = 336 trials). **C,** Odor frequency discrimination accuracy using 1-D CNNs as a function of PYR population size for control variants across three odor conditions (Odor A, Odor B, and Odor Mix). Solid lines represents the mean, and the shaded region represents the standard deviation (n = 144 iterations). **D,** Odor frequency decoding accuracy as a function of PYR population size for knockout models across the same three odor conditions. Solid lines and shaded regions are defined as in Fig. 9**C** (n = 144 iterations).

Figure S1. Biophysical models of different piriform cortex neuron types. **A,** Schematic representation of a pyramidal neuron (PYR) model, consisting of a somatic compartment and five dendritic sections arranged from bottom to top. The model incorporates sodium (Na^+), delayed rectifier potassium (K^+), and leak ion channels, with their respective maximal conductance (gmax) and reversal potentials (E) indicated. **B,** Schematic of a single-compartment feedforward interneuron (FFIN) model. **C**, Schematic of a single-compartment feedback interneuron (FBIN) model, with the respective peak conductances and reversal potentials of the Na^+, K^+, and leak ion channels indicated.

Figure S2. Electrophysiological properties of a pyramidal neuron model. **A,** Step current injections vs. resulting voltage responses from soma and five dendrites (Dend_sec1 to Dend_sec5). **B,** Measured steady-state voltage changes in the soma and dendritic sections as a function of injected current. The slope of linear regression for each trace gives the input resistance of the corresponding compartment. **C,** Action potentials evoked at suprathreshold current in each of the soma and dendritic sections. **D,**

This panel shows the mean spontaneous firing frequency (means ± SD) recorded from each section across the trials (n = 100). **E,** Plot of firing frequency vs. current step amplitude across all compartments. **F,** Example voltage vs. time traces of spontaneous activity recorded from soma and each dendritic section.

Figure S3. Electrophysiological properties of a feedforward interneuron model (FFIN). **A,** Voltage responses recorded from the soma in response to 3 different step current injections (I to III). **B,** (I), Step current injections in the soma. (II), Corresponding voltage responses recorded from the soma. (III), Plot of change in voltage vs. injected current and its linear regression analysis to obtain the corresponding input resistance. **C,** Plot of an action potential recorded from the soma (I) and the corresponding phase plot (II). **D,** Plot of firing frequency vs. current step amplitude. **E,** Example voltage traces of spontaneous activity recorded from the soma. **F,** Average spontaneous firing frequency (means ± SD) recorded across the trials (n = 100).

Figure S4. Electrophysiological properties of a feedback interneuron model (FBIN). **A,** Voltage responses recorded from the soma in response to step current injections (I to III). **B,** (I), Step current injections in the soma. (II), Corresponding voltage responses recorded from the soma. (III), Plot of change in voltage vs. injected current and its linear regression analysis to obtain the corresponding input resistance. **C,** Plot of an action potential recorded from the soma (I) and the corresponding phase plot (II). **D,** Plot of firing frequency vs. current step amplitude. **E,** Example voltage traces of spontaneous activity recorded from the soma. **F,** Average spontaneous firing frequency (means ± SD) recorded across the trials (n = 100).

Figure S5. Decoding odor-frequency from baseline activity under various synaptic knockout conditions. Bar plots show 1-D CNNs' classification accuracies for discriminating 2Hz vs. 20Hz odor conditions using only pre-stimulus/baseline (0–2s) firing activity of all pyramidal neurons, alongside corresponding shuffle controls. Each panel represents a distinct synaptic disconnection: (**A**) Control, (**B**) without FF–PYR, (**C**) without FB–PYR, (**D**) without FF–FF, (**E**) without FB–FB, (**F**) without FF–FF and FB–FB, and (**G**) without PYR–PYR. Accuracy is reported across three odor conditions (A, B, and Mix), with each condition evaluated over 144 iterations using a random 60%/40% train-test split.

Classification performance using activity was statistically compared to chance-level decoding (shuffle condition) using a two-tailed t-test ($p < 0.05$, $n = 144$).

Figure S6. Decoding accuracy as a function of pyramidal neuron (PYR) population size across control and knockout models using logistic regression classifiers. Mean classification accuracy for odor frequency discrimination (2Hz vs. 20Hz) for odors A, B, and Mix (left to right) is plotted against the number of neurons included in the analysis. Accuracy values were averaged across 144 iterations of random neuron subsampling (population step size = 25). Shaded regions represent ± SD. Chance-level performance was estimated by shuffling the trial labels. The logistic regression classifier was trained and tested for all the different networks; without FF-PYR connections (Wo FF-PYR), without FB-PYR connections (Wo FB-PYR), without FF-FF connections (Wo FF-FF), without FB-FB connections (Wo FB-FB), without FF-FF & FB-FB connections (Wo FF-FF & FB-FB) and without PYR-PYR connections (Wo PYR-PYR) (Top to Bottom)). The accuracy plot for the control network has been re-plotted in all the graphs for visual appreciation.

Figure S7. Receiver operating characteristic (ROC) curves comparing the classification performance of 1-D convolutional neural network models (CNN; blue) and logistic regression classifiers (LRC; green) in decoding odor stimulation frequency (2Hz vs. 20Hz) for odor A (left), odor B (middle), and odor Mix (right) in control and knockout models (without FB-PYR connections (Wo FB-PYR), without FF-PYR connections (Wo FF-PYR), without FF-FF connections (Wo FF-FF), without FB-FB connections (Wo FB-FB), without FF-FF & FB-FB connections (Wo FF-FF&FB-FB) and without PYR-PYR connections (Wo PYR-PYR) (Top to Bottom)). The true positive rate (TPR) is plotted against the false positive rate (FPR) across decision thresholds (n = 144 iterations, pyramidal neuron population size = 500). The area under the ROC curve (AUC) quantifies overall decoding performance, with values near 0.5 indicating chance level and values approaching 1.0 indicating perfect discrimination. AUC is quantified for CNNs and classifiers as mean ± SD ($n = 144$ for each). The dashed diagonal line denotes chance-level performance (AUC = 0.5).

Figure 1

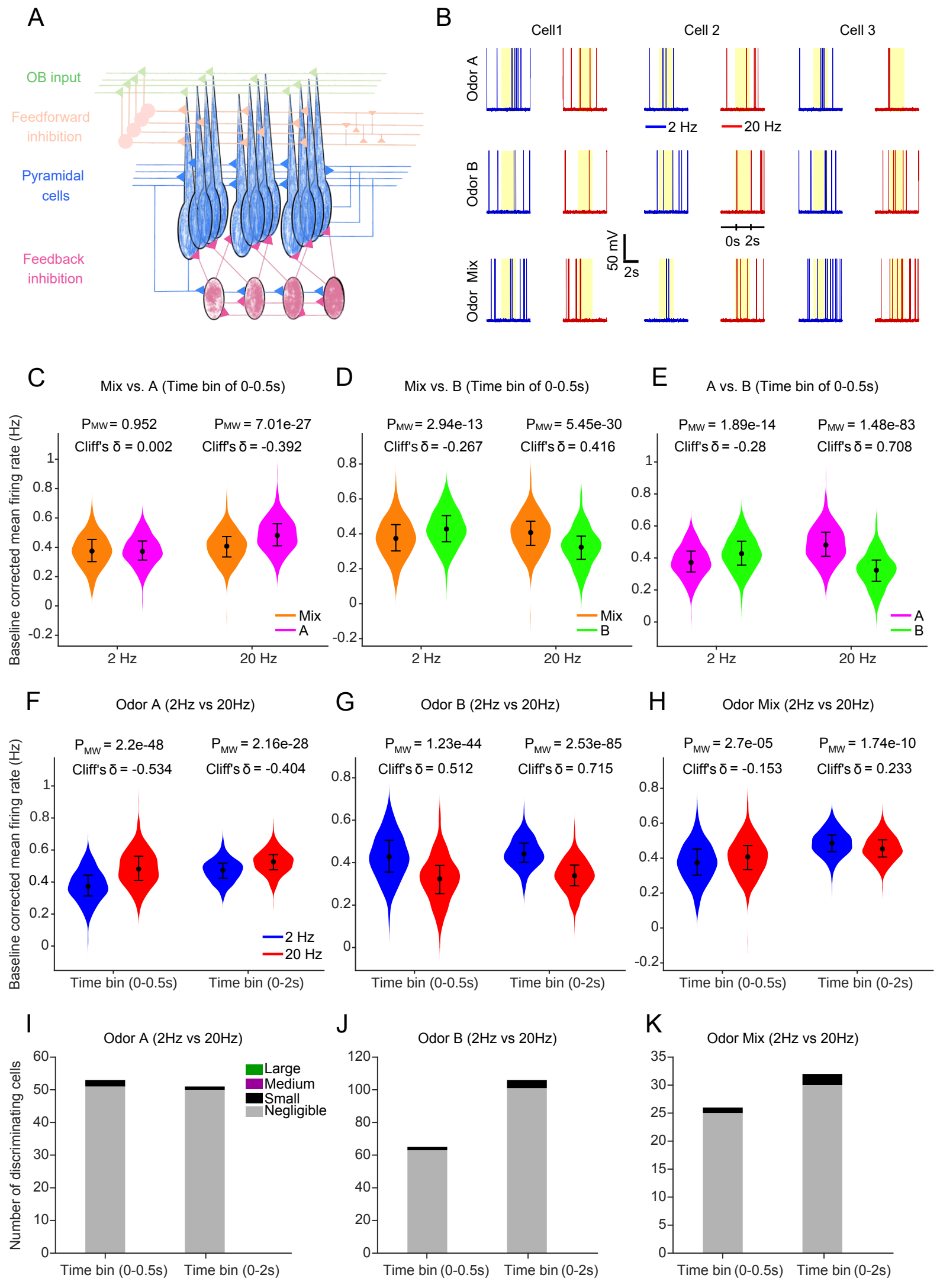
A
OB input
Feedforward inhibition
Pyramidal cells
Feedback inhibition
B
Cell1
Cell 2
Cell 3
Odor A
Odor B
Odor Mix
2 Hz
20 Hz
50 mV
2s
0s 2s
C
Mix vs. A (Time bin of 0-0.5s)
PMW = 0.952
Cliff's δ = 0.002
PMW = 7.01e-27
Cliff's δ = -0.392
Baseline corrected mean firing rate (Hz)
Mix
A
2 Hz
20 Hz
D
Mix vs. B (Time bin of 0-0.5s)
PMW = 2.94e-13
Cliff's δ = -0.267
PMW = 5.45e-30
Cliff's δ = 0.416
Mix
B
E
A vs. B (Time bin of 0-0.5s)
PMW = 1.89e-14
Cliff's δ = -0.28
PMW = 1.48e-83
Cliff's δ = 0.708
A
B
F
Odor A (2Hz vs 20Hz)
PMW = 2.2e-48
Cliff's δ = -0.534
PMW = 2.16e-28
Cliff's δ = -0.404
Baseline corrected mean firing rate (Hz)
2 Hz
20 Hz
Time bin (0-0.5s)
Time bin (0-2s)
G
Odor B (2Hz vs 20Hz)
PMW = 1.23e-44
Cliff's δ = 0.512
PMW = 2.53e-85
Cliff's δ = 0.715
H
Odor Mix (2Hz vs 20Hz)
PMW = 2.7e-05
Cliff's δ = -0.153
PMW = 1.74e-10
Cliff's δ = 0.233
I
Odor A (2Hz vs 20Hz)
Number of discriminating cells
Large
Medium
Small
Negligible
J
Odor B (2Hz vs 20Hz)
K
Odor Mix (2Hz vs 20Hz)

Figure 2

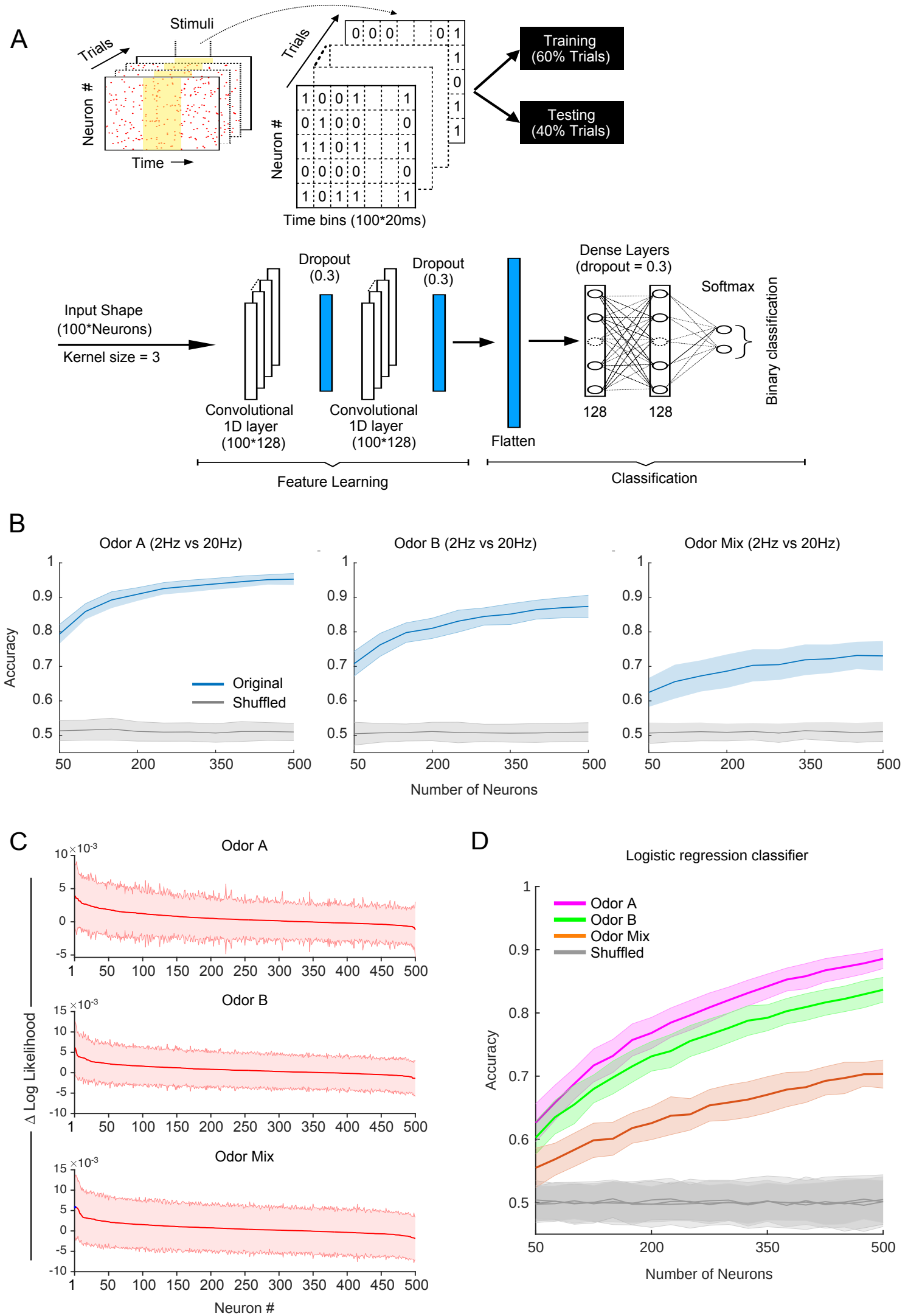
A
Stimuli
Trials
Neuron #
Time
Trials
Neuron #
Time bins (100*20ms)
Training
(60% Trials)
Testing
(40% Trials)
Input Shape
(100*Neurons)
Kernel size = 3
Convolutional
1D layer
(100*128)
Dropout
(0.3)
Convolutional
1D layer
(100*128)
Dropout
(0.3)
Flatten
Dense Layers
(dropout = 0.3)
128
128
Softmax
Binary classification
Feature Learning
Classification
B
Odor A (2Hz vs 20Hz)
Odor B (2Hz vs 20Hz)
Odor Mix (2Hz vs 20Hz)
Accuracy
Original
Shuffled
Number of Neurons
C
Odor A
Odor B
Odor Mix
Δ Log Likelihood
Neuron #
D
Logistic regression classifier
Odor A
Odor B
Odor Mix
Shuffled
Accuracy
Number of Neurons

Figure 3

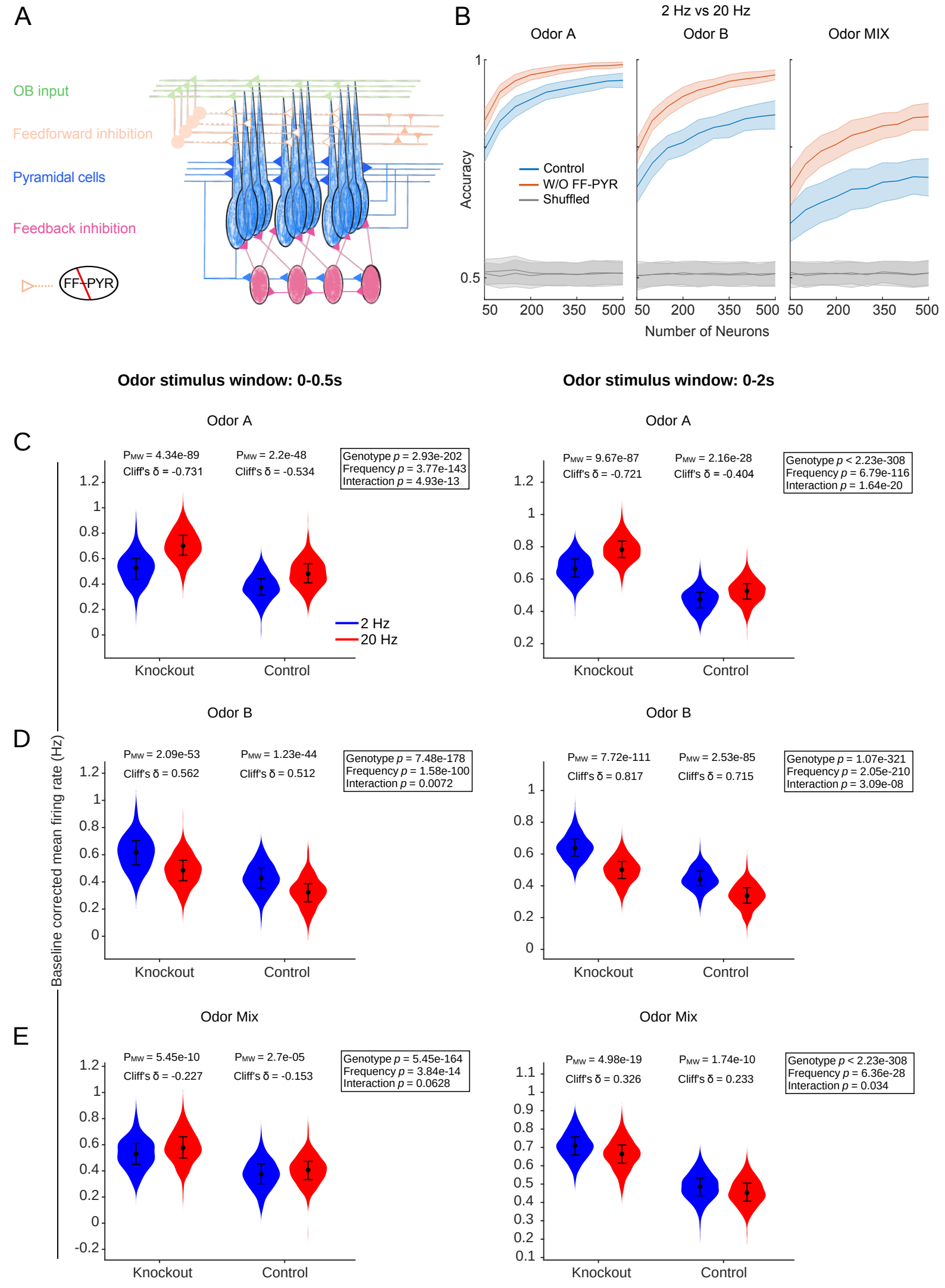
A
OB input
Feedforward inhibition
Pyramidal cells
Feedback inhibition
FF-PYR
B
2 Hz vs 20 Hz
Odor A
Odor B
Odor MIX
Accuracy
Control
W/O FF-PYR
Shuffled
Number of Neurons
Odor stimulus window: 0-0.5s
Odor stimulus window: 0-2s
C
Odor A
PMW = 4.34e-89
Cliff's δ = -0.731
PMW = 2.2e-48
Cliff's δ = -0.534
Genotype p = 2.93e-202
Frequency p = 3.77e-143
Interaction p = 4.93e-13
PMW = 9.67e-87
Cliff's δ = -0.721
PMW = 2.16e-28
Cliff's δ = -0.404
Genotype p < 2.23e-308
Frequency p = 6.79e-116
Interaction p = 1.64e-20
2 Hz
20 Hz
Knockout
Control
D
Odor B
PMW = 2.09e-53
Cliff's δ = 0.562
PMW = 1.23e-44
Cliff's δ = 0.512
Genotype p = 7.48e-178
Frequency p = 1.58e-100
Interaction p = 0.0072
PMW = 7.72e-111
Cliff's δ = 0.817
PMW = 2.53e-85
Cliff's δ = 0.715
Genotype p = 1.07e-321
Frequency p = 2.05e-210
Interaction p = 3.09e-08
Baseline corrected mean firing rate (Hz)
E
Odor Mix
PMW = 5.45e-10
Cliff's δ = -0.227
PMW = 2.7e-05
Cliff's δ = -0.153
Genotype p = 5.45e-164
Frequency p = 3.84e-14
Interaction p = 0.0628
PMW = 4.98e-19
Cliff's δ = 0.326
PMW = 1.74e-10
Cliff's δ = 0.233
Genotype p < 2.23e-308
Frequency p = 6.36e-28
Interaction p = 0.034

Figure 4

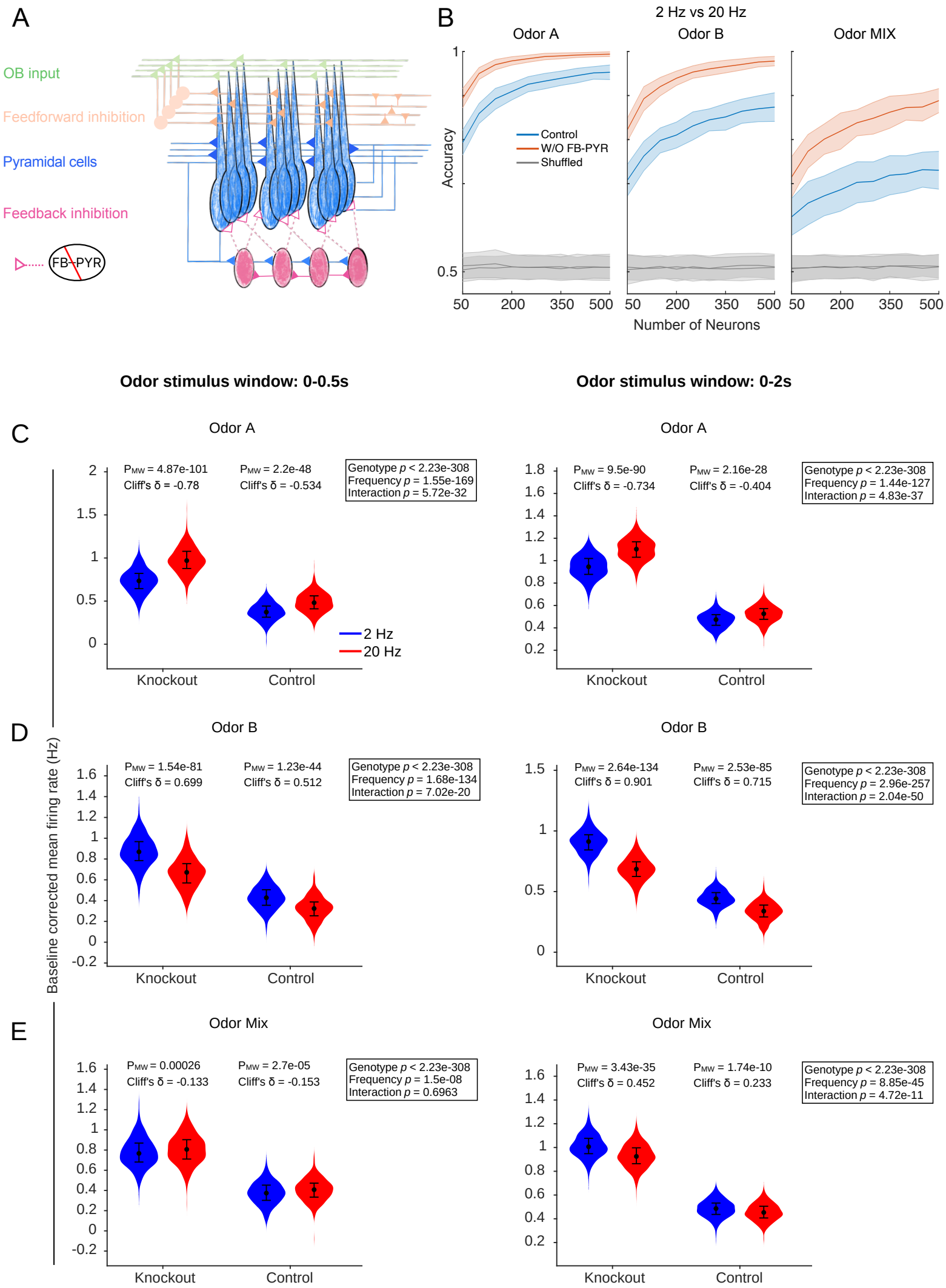
A
OB input
Feedforward inhibition
Pyramidal cells
Feedback inhibition
FB-PYR
B
2 Hz vs 20 Hz
Odor A
Odor B
Odor MIX
Accuracy
Control
W/O FB-PYR
Shuffled
Number of Neurons
Odor stimulus window: 0-0.5s
Odor stimulus window: 0-2s
C
Odor A
PMW = 4.87e-101
Cliff's δ = -0.78
PMW = 2.2e-48
Cliff's δ = -0.534
Genotype p < 2.23e-308
Frequency p = 1.55e-169
Interaction p = 5.72e-32
2 Hz
20 Hz
PMW = 9.5e-90
Cliff's δ = -0.734
PMW = 2.16e-28
Cliff's δ = -0.404
Genotype p < 2.23e-308
Frequency p = 1.44e-127
Interaction p = 4.83e-37
D
Odor B
PMW = 1.54e-81
Cliff's δ = 0.699
PMW = 1.23e-44
Cliff's δ = 0.512
Genotype p < 2.23e-308
Frequency p = 1.68e-134
Interaction p = 7.02e-20
PMW = 2.64e-134
Cliff's δ = 0.901
PMW = 2.53e-85
Cliff's δ = 0.715
Genotype p < 2.23e-308
Frequency p = 2.96e-257
Interaction p = 2.04e-50
E
Odor Mix
PMW = 0.00026
Cliff's δ = -0.133
PMW = 2.7e-05
Cliff's δ = -0.153
Genotype p < 2.23e-308
Frequency p = 1.5e-08
Interaction p = 0.6963
PMW = 3.43e-35
Cliff's δ = 0.452
PMW = 1.74e-10
Cliff's δ = 0.233
Genotype p < 2.23e-308
Frequency p = 8.85e-45
Interaction p = 4.72e-11
Baseline corrected mean firing rate (Hz)
Knockout
Control

Figure 5

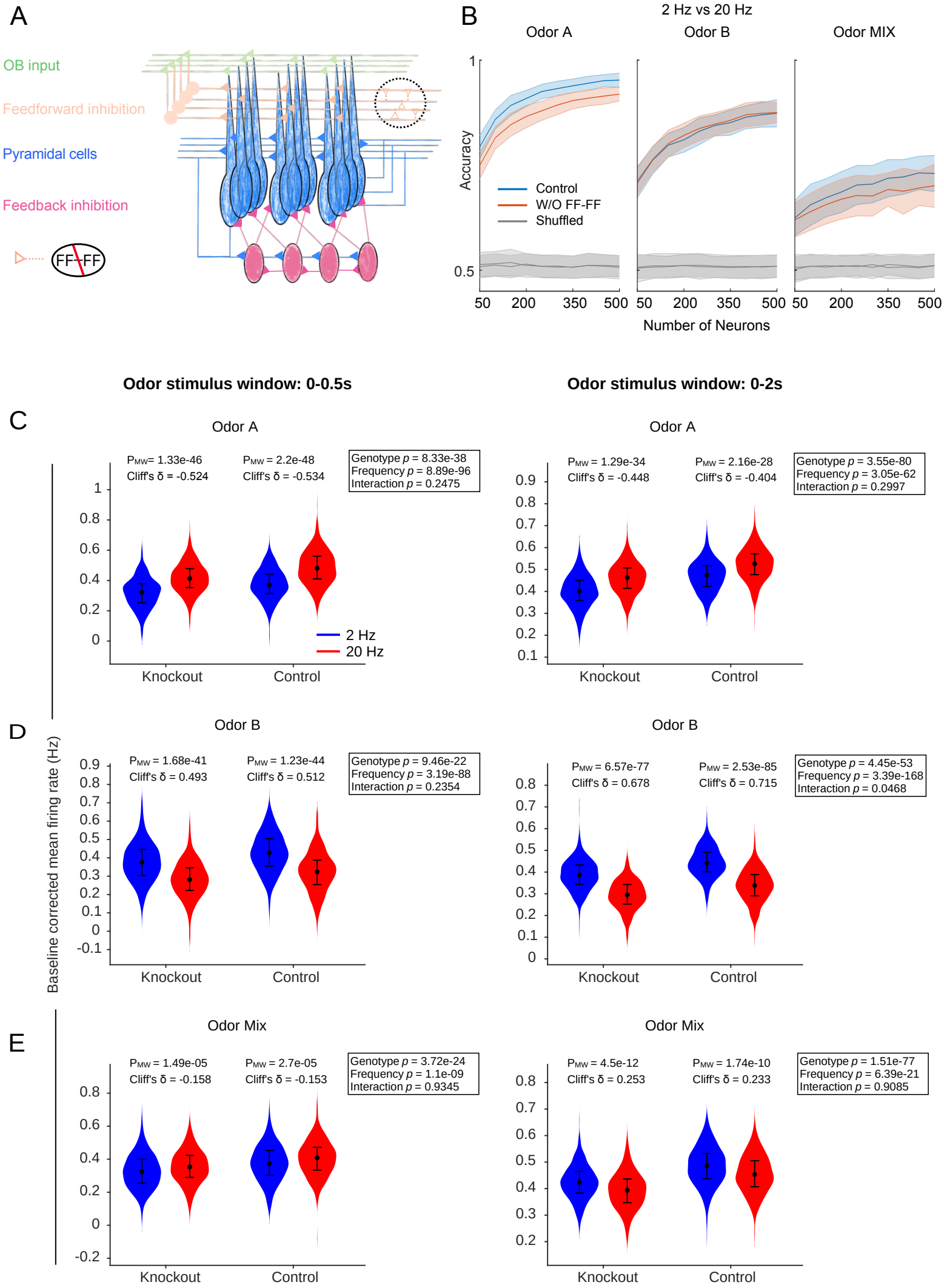
A
OB input
Feedforward inhibition
Pyramidal cells
Feedback inhibition
FF-FF
B
2 Hz vs 20 Hz
Odor A
Odor B
Odor MIX
Accuracy
Control
W/O FF-FF
Shuffled
Number of Neurons
Odor stimulus window: 0-0.5s
Odor stimulus window: 0-2s
C
Odor A
PMW= 1.33e-46
Cliff's δ = -0.524
PMW = 2.2e-48
Cliff's δ = -0.534
Genotype p = 8.33e-38
Frequency p = 8.89e-96
Interaction p = 0.2475
2 Hz
20 Hz
Knockout
Control
PMW = 1.29e-34
Cliff's δ = -0.448
PMW = 2.16e-28
Cliff's δ = -0.404
Genotype p = 3.55e-80
Frequency p = 3.05e-62
Interaction p = 0.2997
D
Odor B
PMW = 1.68e-41
Cliff's δ = 0.493
PMW = 1.23e-44
Cliff's δ = 0.512
Genotype p = 9.46e-22
Frequency p = 3.19e-88
Interaction p = 0.2354
PMW = 6.57e-77
Cliff's δ = 0.678
PMW = 2.53e-85
Cliff's δ = 0.715
Genotype p = 4.45e-53
Frequency p = 3.39e-168
Interaction p = 0.0468
Baseline corrected mean firing rate (Hz)
E
Odor Mix
PMW = 1.49e-05
Cliff's δ = -0.158
PMW = 2.7e-05
Cliff's δ = -0.153
Genotype p = 3.72e-24
Frequency p = 1.1e-09
Interaction p = 0.9345
PMW = 4.5e-12
Cliff's δ = 0.253
PMW = 1.74e-10
Cliff's δ = 0.233
Genotype p = 1.51e-77
Frequency p = 6.39e-21
Interaction p = 0.9085

Figure 6

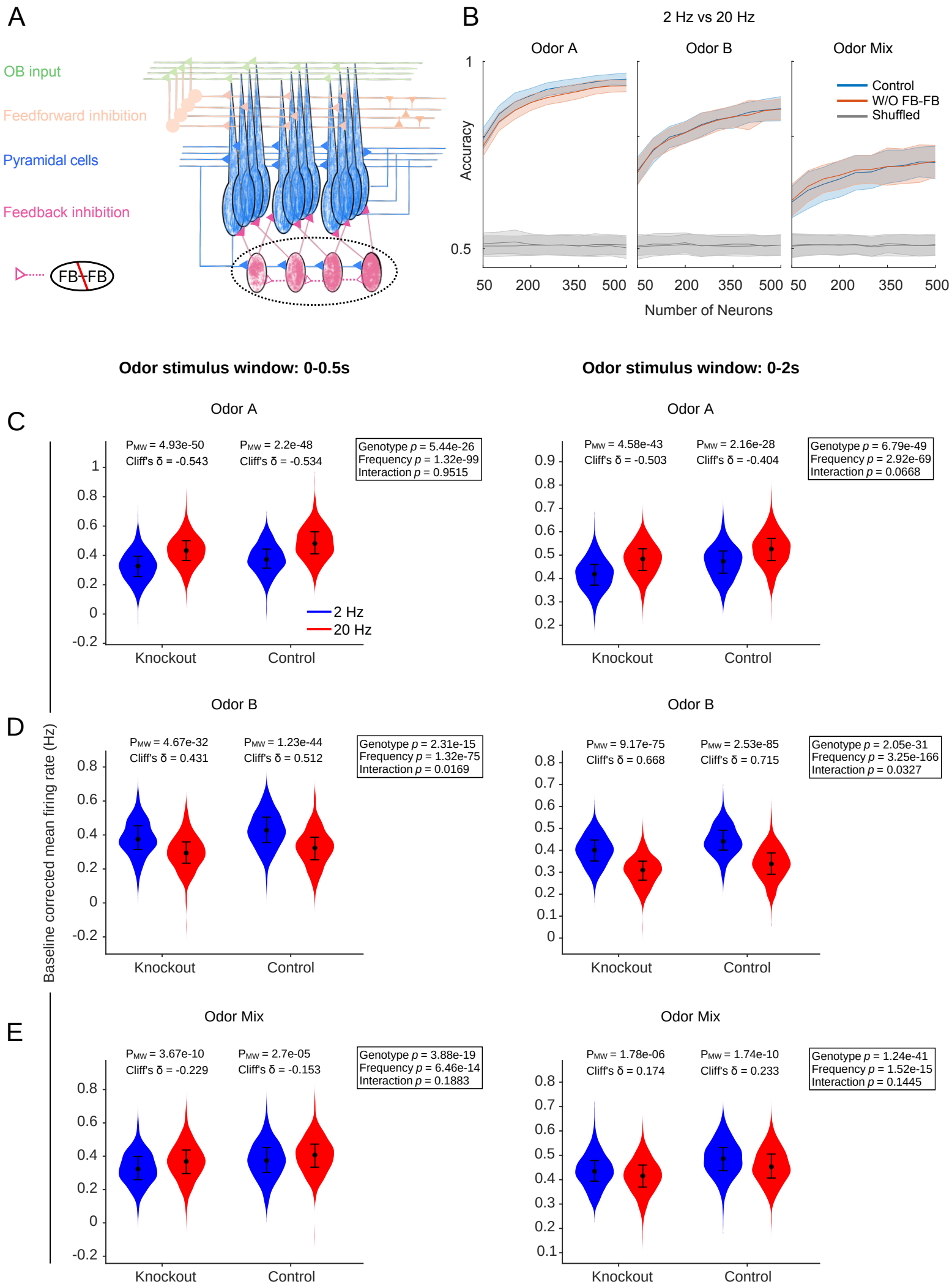
A
OB input
Feedforward inhibition
Pyramidal cells
Feedback inhibition
FB
FB
B
2 Hz vs 20 Hz
Odor A
Odor B
Odor Mix
Control
W/O FB-FB
Shuffled
Accuracy
1
0.5
50
200
350
500
Number of Neurons
Odor stimulus window: 0-0.5s
Odor stimulus window: 0-2s
C
Odor A
PMW = 4.93e-50
Cliff's δ = -0.543
PMW = 2.2e-48
Cliff's δ = -0.534
Genotype p = 5.44e-26
Frequency p = 1.32e-99
Interaction p = 0.9515
2 Hz
20 Hz
Knockout
Control
PMW = 4.58e-43
Cliff's δ = -0.503
PMW = 2.16e-28
Cliff's δ = -0.404
Genotype p = 6.79e-49
Frequency p = 2.92e-69
Interaction p = 0.0668
D
Odor B
PMW = 4.67e-32
Cliff's δ = 0.431
PMW = 1.23e-44
Cliff's δ = 0.512
Genotype p = 2.31e-15
Frequency p = 1.32e-75
Interaction p = 0.0169
PMW = 9.17e-75
Cliff's δ = 0.668
PMW = 2.53e-85
Cliff's δ = 0.715
Genotype p = 2.05e-31
Frequency p = 3.25e-166
Interaction p = 0.0327
Baseline corrected mean firing rate (Hz)
E
Odor Mix
PMW = 3.67e-10
Cliff's δ = -0.229
PMW = 2.7e-05
Cliff's δ = -0.153
Genotype p = 3.88e-19
Frequency p = 6.46e-14
Interaction p = 0.1883
PMW = 1.78e-06
Cliff's δ = 0.174
PMW = 1.74e-10
Cliff's δ = 0.233
Genotype p = 1.24e-41
Frequency p = 1.52e-15
Interaction p = 0.1445

Figure 7

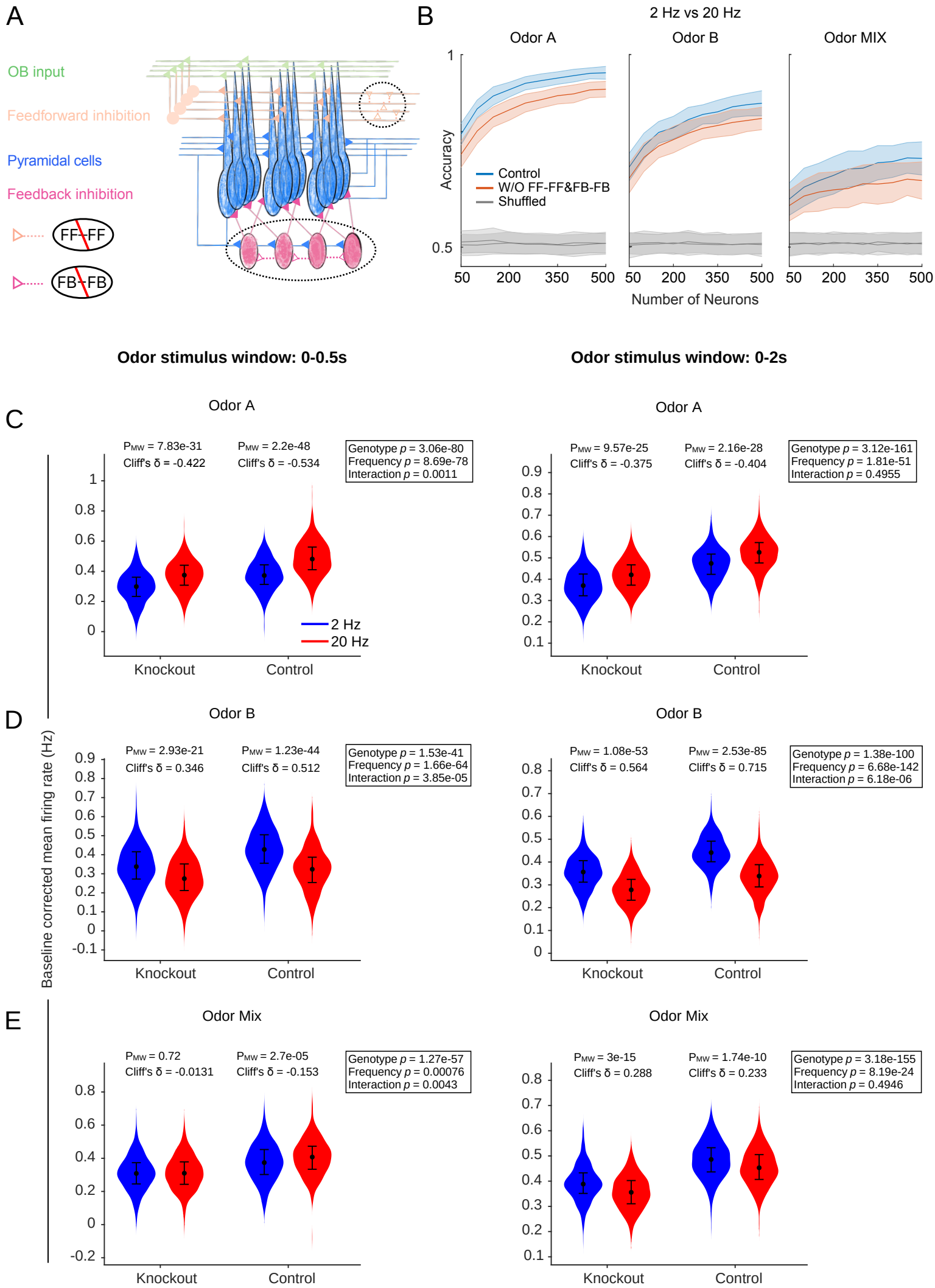
A
OB input
Feedforward inhibition
Pyramidal cells
Feedback inhibition
FF-FF
FB-FB
B
2 Hz vs 20 Hz
Odor A
Odor B
Odor MIX
Accuracy
Control
W/O FF-FF&FB-FB
Shuffled
Number of Neurons
Odor stimulus window: 0-0.5s
Odor stimulus window: 0-2s
C
Odor A
PMW = 7.83e-31
Cliff's δ = -0.422
PMW = 2.2e-48
Cliff's δ = -0.534
Genotype p = 3.06e-80
Frequency p = 8.69e-78
Interaction p = 0.0011
2 Hz
20 Hz
Knockout
Control
PMW = 9.57e-25
Cliff's δ = -0.375
PMW = 2.16e-28
Cliff's δ = -0.404
Genotype p = 3.12e-161
Frequency p = 1.81e-51
Interaction p = 0.4955
D
Odor B
PMW = 2.93e-21
Cliff's δ = 0.346
PMW = 1.23e-44
Cliff's δ = 0.512
Genotype p = 1.53e-41
Frequency p = 1.66e-64
Interaction p = 3.85e-05
PMW = 1.08e-53
Cliff's δ = 0.564
PMW = 2.53e-85
Cliff's δ = 0.715
Genotype p = 1.38e-100
Frequency p = 6.68e-142
Interaction p = 6.18e-06
Baseline corrected mean firing rate (Hz)
E
Odor Mix
PMW = 0.72
Cliff's δ = -0.0131
PMW = 2.7e-05
Cliff's δ = -0.153
Genotype p = 1.27e-57
Frequency p = 0.00076
Interaction p = 0.0043
PMW = 3e-15
Cliff's δ = 0.288
PMW = 1.74e-10
Cliff's δ = 0.233
Genotype p = 3.18e-155
Frequency p = 8.19e-24
Interaction p = 0.4946

Figure 8

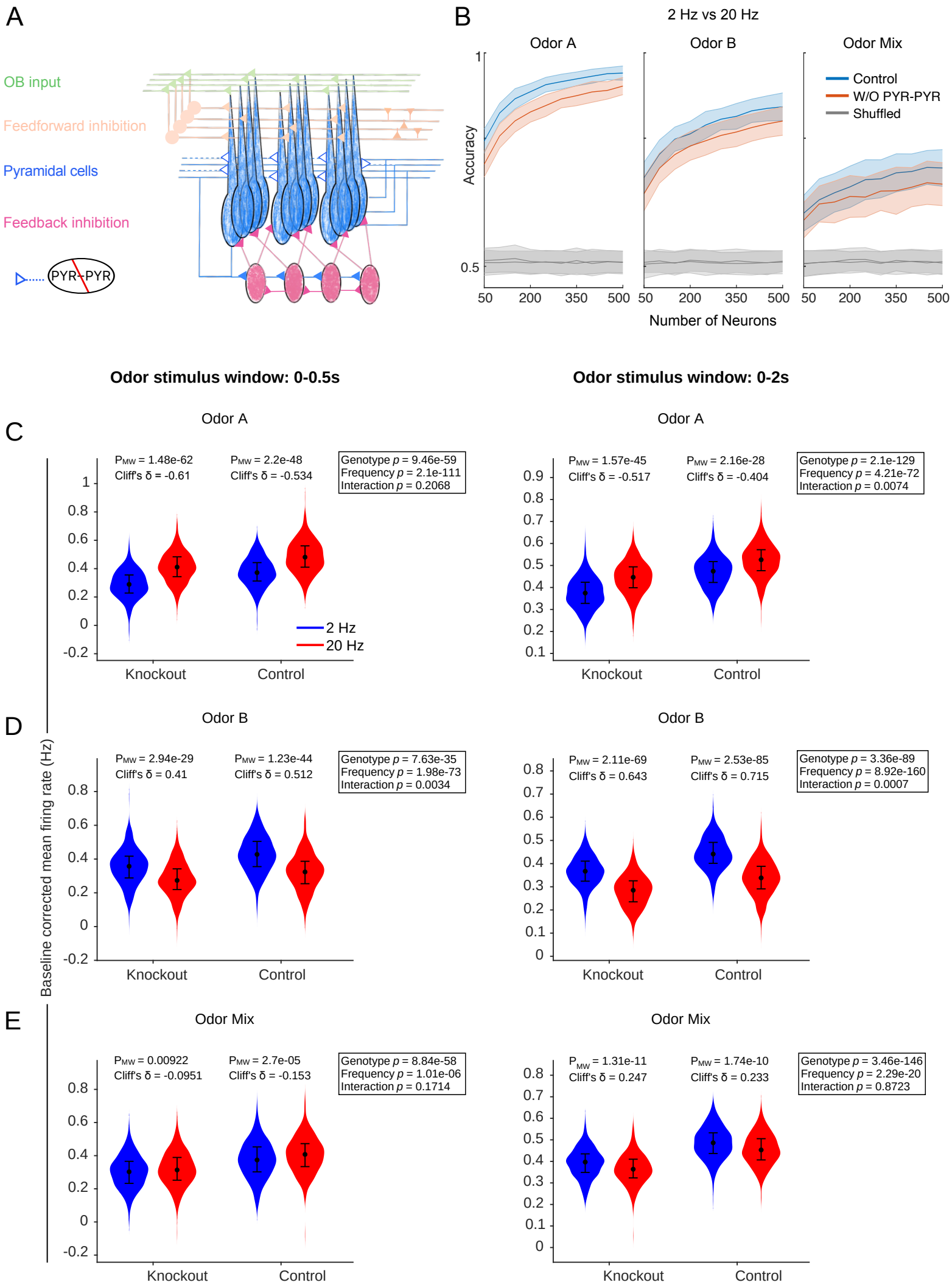
A
OB input
Feedforward inhibition
Pyramidal cells
Feedback inhibition
PYR-PYR
B
2 Hz vs 20 Hz
Odor A
Odor B
Odor Mix
Control
W/O PYR-PYR
Shuffled
Accuracy
Number of Neurons
Odor stimulus window: 0-0.5s
Odor stimulus window: 0-2s
C
D
E
Odor A
Odor B
Odor Mix
Baseline corrected mean firing rate (Hz)
2 Hz
20 Hz
Knockout
Control
PMW = 1.48e-62
Cliff's δ = -0.61
PMW = 2.2e-48
Cliff's δ = -0.534
Genotype p = 9.46e-59
Frequency p = 2.1e-111
Interaction p = 0.2068
PMW = 1.57e-45
Cliff's δ = -0.517
PMW = 2.16e-28
Cliff's δ = -0.404
Genotype p = 2.1e-129
Frequency p = 4.21e-72
Interaction p = 0.0074
PMW = 2.94e-29
Cliff's δ = 0.41
PMW = 1.23e-44
Cliff's δ = 0.512
Genotype p = 7.63e-35
Frequency p = 1.98e-73
Interaction p = 0.0034
PMW = 2.11e-69
Cliff's δ = 0.643
PMW = 2.53e-85
Cliff's δ = 0.715
Genotype p = 3.36e-89
Frequency p = 8.92e-160
Interaction p = 0.0007
PMW = 0.00922
Cliff's δ = -0.0951
PMW = 2.7e-05
Cliff's δ = -0.153
Genotype p = 8.84e-58
Frequency p = 1.01e-06
Interaction p = 0.1714
PMW = 1.31e-11
Cliff's δ = 0.247
PMW = 1.74e-10
Cliff's δ = 0.233
Genotype p = 3.46e-146
Frequency p = 2.29e-20
Interaction p = 0.8723

Figure 9

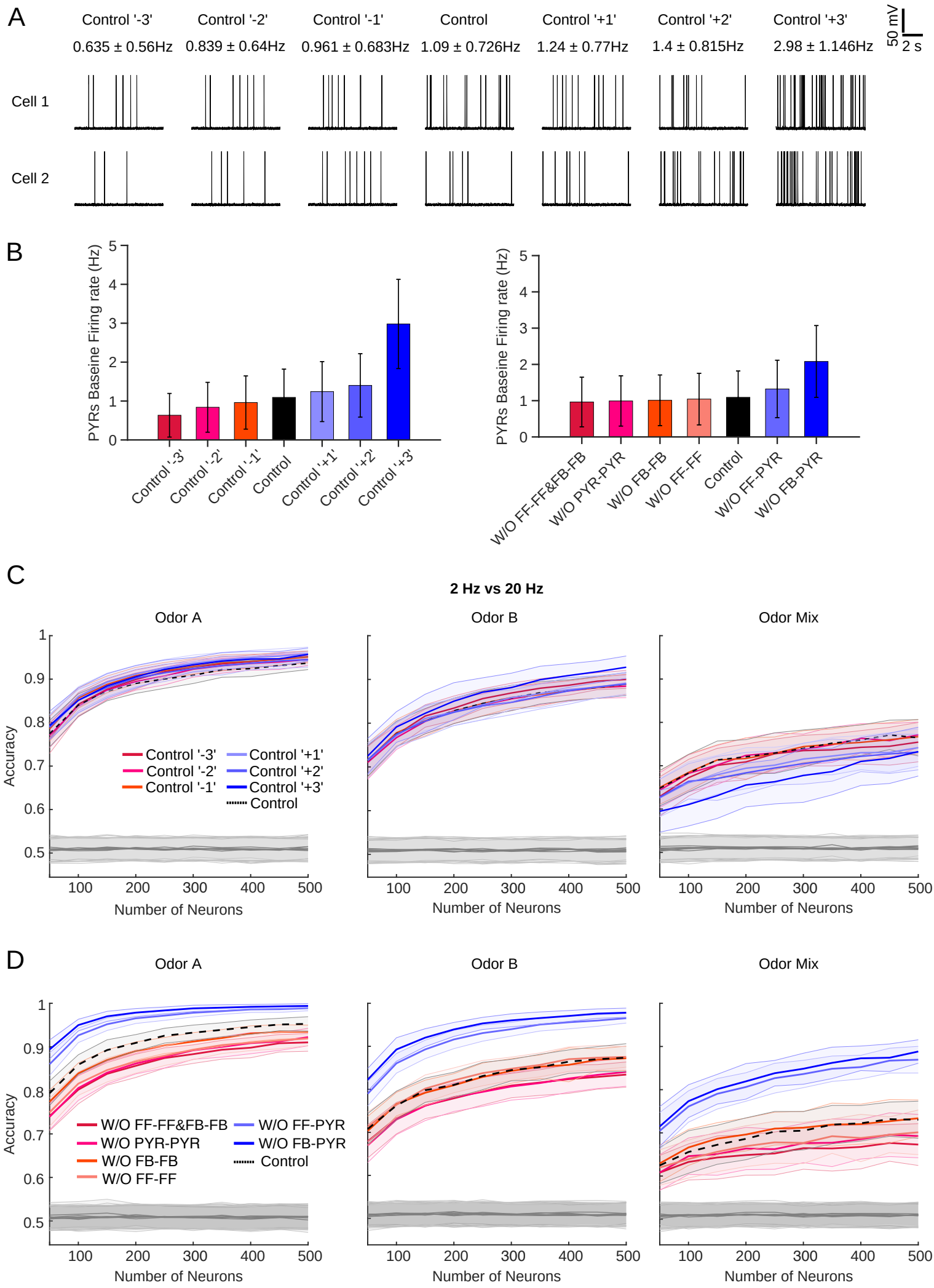
A
Control '-3'
0.635 ± 0.56Hz
Control '-2'
0.839 ± 0.64Hz
Control '-1'
0.961 ± 0.683Hz
Control
1.09 ± 0.726Hz
Control '+1'
1.24 ± 0.77Hz
Control '+2'
1.4 ± 0.815Hz
Control '+3'
2.98 ± 1.146Hz
50 mV
2 s
Cell 1
Cell 2
B
PYRs Baseine Firing rate (Hz)
Control '-3'
Control '-2'
Control '-1'
Control
Control '+1'
Control '+2'
Control '+3'
W/O FF-FF&FB-FB
W/O PYR-PYR
W/O FB-FB
W/O FF-FF
W/O FF-PYR
W/O FB-PYR
C
2 Hz vs 20 Hz
Odor A
Odor B
Odor Mix
Accuracy
Number of Neurons
D
W/O FF-FF&FB-FB
W/O PYR-PYR
W/O FB-FB
W/O FF-FF
W/O FF-PYR
W/O FB-PYR
Control

Table 1. Morphological and biophysical parameters of the modeled cells of the piriform cortex.

Parameters	PYR						FFIN	FBIN
	Soma	Dend1	Dend2	Dend3	Dend4	Dend5	Soma	Soma
Input Resistance (MΩ)	79.84	80.28	84.94	99.36	137.58	246.18	93.36	50.29
Avg. spontaneous firing rate (mean ± std) (Hz)	2.22±0.98	2.21±1.27	2.32±1.2	2.19±1.16	2.2±1.4	2.67±1.59	2±1.14	6.55±2.11
Length (µm)	100	100	100	100	100	100	85	68
Diameter (µm)	29	2.57	1.77	1.2	0.8	0.5	85	68

Table 2. Model parameters

Synaptic Connections	Synaptic Weight	EPSP/IPSP (mV)	Tau1 (ms)	Tau2 (ms)	E_N (mV)	Synaptic Latency (ms)	Connection Probability
PYR-PYR DEND 1	0.00002	0.12	0.24	3.6	0	1.54	0.2
PYR-PYR DEND 2	0.00002	0.11	0.24	3.6	0	1.54	
PYR-PYR DEND 3	0.00002	0.11	0.24	3.6	0	1.54	
PYR-PYR DEND 4	0.00002	0.11	0.24	3.6	0	1.54	
FBIN-PYR SOMA	0.007	1.9	0.2	1.2	-80	0.65	0.35
FFIN-PYR DEND 4	0.007	1.4	0.2	1.2	-80	0.6	0.3
FFIN-PYR DEND 5	0.007	0.95	0.2	1.2	-80	0.6	
FBIN-FBIN	0.06	1.5	0.2	1.2	-80	1.54	0.1
PYR-FBIN	0.0001	0.31	0.26	9	0	0.65	0.18
M/T-PYR DEND 5	0.000037	0.19	0.2	1.2	0	1.27	0.2
M/T-FFIN	0.00015	0.59	0.2	1.2	0	2.42	0.4
FFIN-FFIN	0.0095	3	0.2	1.2	-80	1.54	0.4

Table 3. Highlighted p-values of contrasts using ART procedure followed by Anova.

Knockout Type	Effect	Bin 1 (0-0.5s)			Bin 4 (0-2s)		
		Odor A	**Odor B**	**Odor Mix**	**Odor A**	**Odor B**	**Odor Mix**
W/O FF-PYR	Control vs Knockout	8.043E-233	3.783E-210	2.075E-193	<2.225E-308	<2.225E-308	<2.225E-308
	2Hz vs 20Hz	3.290E-160	4.600E-108	3.957E-14	3.094E-125	2.727E-241	6.362E-28
	Interaction	2.173E-13	0.007	0.064	8.782E-21	1.934E-08	0.035
W/O FB-PYR	Control vs Knockout	<2.225E-308	<2.225E-308	<2.225E-308	<2.225E-308	<2.225E-308	<2.225E-308
	2Hz vs 20Hz	2.406E-186	5.566E-147	1.531E-08	4.979E-139	8.252E-299	5.914E-47
	Interaction	3.175E-32	3.899E-20	0.696	5.523E-38	3.951E-52	2.648E-11
W/O FF-FF	Control vs Knockout	1.847E-39	1.606E-22	2.104E-25	2.680E-87	4.795E-55	9.072E-82
	2Hz vs 20Hz	1.376E-100	1.618E-90	1.572E-09	6.222E-65	2.258E-187	3.322E-21
	Interaction	0.251	0.242	0.935	0.298	0.046	0.908
W/O FB-FB	Control vs Knockout	3.640E-27	8.862E-16	1.524E-20	9.234E-52	1.844E-32	8.313E-44
	2Hz vs 20Hz	5.111E-105	1.414E-81	6.524E-14	6.357E-74	5.794E-185	1.195E-15
	Interaction	0.952	0.015	0.190	0.063	0.031	0.144
W/O FF-FF&FB-FB	Control vs Knockout	9.251E-85	4.542E-43	6.043E-60	6.364E-179	1.168E-107	1.159E-172
	2Hz vs 20Hz	4.904E-82	2.701E-66	0.0007	2.570E-53	9.577E-156	3.415E-24
	Interaction	0.001	4.502E-05	0.004	0.495	5.955E-06	0.494
W/O PYR-PYR	Control vs Knockout	5.786E-63	8.046E-37	3.543E-61	1.954E-142	8.882E-95	7.569E-161
	2Hz vs 20Hz	1.030E-119	1.443E-77	9.210E-07	1.479E-76	3.659E-177	1.159E-20
	Interaction	0.207	0.003	0.169	0.007	0.0007	0.872

Table 4. AUC values of ROC curves over 144 trials.

Network Model	1-D CNN Models			Logistic Regression Classifier		
	Odor A	Odor B	Odor Mix	Odor A	Odor B	Odor Mix
CONTROL	0.992 ± 0.003	0.953 ± 0.018	0.813 ± 0.044	0.895 ± 0.018	0.846 ± 0.020	0.720 ± 0.024
Wo FF-PYR	0.999 ± 0.001	0.995 ± 0.003	0.946 ± 0.019	0.971 ± 0.009	0.945 ± 0.013	0.814 ± 0.023
Wo FB-PYR	1.0	0.998 ± 0.002	0.958 ± 0.020	0.987 ± 0.006	0.976 ± 0.009	0.888 ± 0.018
Wo FF-FF	0.978 ± 0.008	0.954 ± 0.015	0.781 ± 0.042	0.865 ± 0.017	0.832 ± 0.021	0.690 ± 0.026
Wo FB-FB	0.986 ± 0.006	0.949 ± 0.017	0.822 ± 0.042	0.865 ± 0.018	0.832 ± 0.020	0.715 ± 0.027
Wo FF-FF&FB-FB	0.973 ± 0.010	0.914 ± 0.022	0.749 ± 0.054	0.860 ± 0.019	0.791 ± 0.021	0.648 ± 0.025
Wo PYR-PYR	0.977 ± 0.010	0.922 ± 0.026	0.768 ± 0.053	0.823 ± 0.020	0.798 ± 0.022	0.664 ± 0.027

Table 5. Pyramidal population's baseline firing rate (Hz).

W/O FF-FF&FB-FB	W/O PYR-PYR	W/O FB-FB	W/O FF-FF	CONTROL	W/O FF-PYR	W/O FB-PYR
0.963 ± 0.683	0.992 ± 0.692	1.01 ± 0.699	1.04 ± 0.711	1.09 ± 0.726	1.32 ± 0.792	2.08 ± 0.991
Control '-3'	Control '-2'	Control '-1'	Control	Control '+1'	Control '+2'	Control '+3'
0.635 ± 0.561	0.839 ± 0.641	0.961 ± 0.683	1.09 ± 0.726	1.24 ± 0.771	1.4 ± 0.815	2.98 ± 1.146